

PIONIC X RAYS FROM ^{12}C AND ^{13}C

by

CHARLES ALAN FRY

B.Sc., University of Victoria, 1976

A THESIS SUBMITTED IN PARTIAL FULFILLMENT

OF THE REQUIREMENTS FOR THE DEGREE OF

MASTER OF SCIENCE

in the Department of

Physics

We accept this thesis as conforming
to the required standard

ACCEPTED
FACULTY OF GRADUATE STUDIES

Dr. R.M. Pearce

Dr. G.A. Beer

Dr. G.R. Branton

Dr. G.R. Mason

DATE

29th Mar 81

DEAN

© Alan Fry, 1980

University of Victoria
June, 1980

All rights reserved. This thesis may not be reproduced
in whole or in part, by mimeograph or other means,
without the permission of the author.

Supervisor: Professor R.M. Pearce

Abstract

The energies and widths of pionic 2p-1s and 3d-2p X rays have been measured in the isotopic pair ^{12}C and ^{13}C .

Values obtained are:

$$^{12}\text{C} \begin{array}{l} 2p-1s \ E = 93.287 (43) \text{ keV}, \ \Gamma = 2.66 (12) \text{ keV;} \\ 3d-2p \ E = 18.400 (6) \text{ keV}, \ \Gamma = 1.17 (11) \text{ eV;} \end{array}$$

$$^{13}\text{C} \begin{array}{l} 2p-1s \ E = 92.227 (27) \text{ keV}, \ \Gamma = 2.59 (11) \text{ keV;} \\ 3d-2p \ E = 18.427 (2) \text{ keV}, \ \Gamma = .97 (10) \text{ eV.} \end{array}$$

There has been no previous measurement of pionic X rays from ^{13}C . We have also measured muonic 2p-1s X-ray energies in ^{12}C and ^{13}C as well as ^{14}N , from which we have calculated the nuclear charge radius. Values obtained are:

$$^{12}\text{C}: \ E = 75.251 (15) \text{ keV}, \ \langle r^2 \rangle^{1/2} = 2.51 (5) \text{ fm};$$

$$^{13}\text{C}: \ E = 75.303 (15) \text{ keV}, \ \langle r^2 \rangle^{1/2} = 2.51 (5) \text{ fm};$$

$$^{14}\text{N}: \ E = 102.392 (4) \text{ keV}, \ \langle r^2 \rangle^{1/2} = 2.579 (3) \text{ fm.}$$

Examiners:


Dr. R.M. Pearce


Dr. G.A. Beer


Dr. G.R. Branton



Dr. G.R. Mason



Table of Contents

	page
Abstract.....	ii
List of Tables.....	vi
List of Figures.....	vii
Acknowledgments.....	ix
Dedication.....	x
Chapter 1, Introduction.....	1
1.1 Exotic Atoms.....	1
1.2 Pionic Atoms.....	1
1.3 Experimentally Measured Quantities.....	3
Chapter 2, The Experimental Arrangement and Technique.....	7
2.1 The Beamline.....	7
2.2 The Experimental Area.....	7
2.2.1 The Scintillator Telescope.....	7
2.2.2 The Degradar and Range Adjustment for Pions.....	10
2.2.3 The Targets.....	12
2.2.4 Shielding.....	12
2.3 The Detection System.....	15
2.3.1 Time of Flight Separation.....	15
2.3.2 The Detector and Accompanying Electronics.....	23
2.3.3 The Computerized Data Acquisition System.....	25
Chapter 3, The Fitting Process.....	27
3.1 Lineshape.....	27
3.1.1 Gaussian.....	27

3.1.2 Lorentzian.....	27
3.1.3 Background.....	28
3.1.4 Efficiency.....	29
3.2 The Best Fit Criterion.....	29
Chapter 4, Calibration.....	31
4.1 Energy Calibration.....	40
4.2 Detector Efficiency.....	43
4.2.1 The Method of Efficiency Determination...	43
4.3 Lineshape.....	50
4.3.1 FWHM.....	50
4.3.2 The Exponential Tailing Parameters, EXT1 and EXT2.....	51
Chapter 5, The Determination of the ^{12}C Contamination in the ^{13}C Spectra.....	53
5.1 Muons.....	54
5.2 Pions.....	55
Chapter 6, The Determination of the πC 2p-1s Energies, Widths, and Strong Interaction Shifts.....	58
6.1 The $\pi^{12}\text{C}$ Fit.....	58
6.2 The $\pi^{13}\text{C}$ Fit.....	61
6.3 Strong Interaction Shifts of the 1s Level in Pionic ^{12}C and ^{13}C	64
Chapter 7, The Determination of the 3d-2p Transition Energy and Width in Pionic ^{12}C and ^{13}C	66
7.1 The 3d-2p Transition Energy in $\pi^{12}\text{C}$ and $\pi^{13}\text{C}$	66
7.2 The Width of the 2p Level in $\pi^{12}\text{C}$ and $\pi^{13}\text{C}$	66

Appendix A, Low Energy Exponential Tailing.....	77
A.1 Mathematical Formulation.....	77
Appendix B, Muonic X-ray 2p-1s Transition Energies and r.m.s. Charge Radii.....	81
Appendix C, Modifications to the FOTRAN code JAGSPOT...	83
C.1 Low Energy Exponential Tailing Function 3.....	83
C.2 Low Energy Exponential Tailing Function 4.....	85
C.3 The LINK Command.....	85
Bibliography.....	87

List of Tables

Table	page
I Measurements of Pionic 2p-1s Energies and Widths in Selected Isotopic Pairs.....	5
II Key to Peak Identities in Figures 2.6, 2.7, and 2.8...	22
III Peaks Used in the Energy Calibration.....	41
IV Linear Energy Calibration.....	42
V Relative Efficiency from ^{182}Ta	45
VI Relative Efficiency from ^{241}Am	46
VII Relative Efficiency from ^{57}Co	46
VIII Constants in the Rational Function $Q(x)$	50
IX Variation of FWHM with Energy.....	51
X Exponential Tailing Parameters Determined by Fits of the $\pi^{12}\text{C}$ and $\pi^{13}\text{C}$ Spectra.....	52
XI Relative Intensities of Various Peaks in the Target-empty and $\pi^{13}\text{C}$ Spectra.....	57
XII Various Contributions to the Uncertainty in the $\pi^{12}\text{C}$ 2p-1s Energy E and Width Γ	62
XIII Various Contributions to the Uncertainty in the $\pi^{13}\text{C}$ 2p-1s Energy E and Width Γ	63
XIV Strong Interaction Shifts.....	65
XV Intensities of Various Transitions Used in the Determination of the 2p Level Width Γ s.....	68

List of Figures

Figure	page
2.1 The Secondary Channel M9.....	8
2.2 The Experimental Area.....	9
2.3 Logic Diagram.....	11
2.4 Range Adjustment.....	13
2.5 The ^{13}C Target.....	14
2.6 a The $\pi^{12}\text{C}$ Spectrum (first part).....	16
b The $\pi^{12}\text{C}$ Spectrum (second part).....	17
2.7 a The $\pi^{13}\text{C}$ Spectrum (first part).....	18
b The $\pi^{13}\text{C}$ Spectrum (second part).....	19
2.8 a The Target-empty Spectrum (first part).....	20
b The Target-empty Spectrum (second part).....	21
2.9 Schematic of a Ge Detector.....	23
4.1 a The ^{13}C Calibration Spectrum (first part).....	32
b The ^{13}C Calibration Spectrum (second part).....	33
4.2 a The ^{12}C Calibration Spectrum (first part).....	34
b The ^{12}C Calibration Spectrum (second part).....	35
4.3 a Spectrum of ^{57}Co and ^{182}Ta (first part).....	36
b Spectrum of ^{57}Co and ^{182}Ta (second part).....	37
4.4 a Spectrum of ^{241}Am and ^{182}Ta (first part).....	38
b Spectrum of ^{241}Am and ^{182}Ta (second part).....	39
4.5 Photon Cross-section for Tantalum.....	47
4.6 Detector Relative Efficiency.....	49
6.1 The $\pi^{12}\text{C}$ 2p-1s Fit.....	59

7.1 The $\pi^{12}\text{C}$ 3d-2p Fit.....	69
7.2 Fit of the $\pi^{12}\text{C}$ L-Series.....	70
7.3 The $\pi^{13}\text{C}$ 3d-2p Fit.....	71
7.4 Fit of the $\pi^{13}\text{C}$ L-Series.....	72
7.5 Photon Cross-section for Carbon.....	73
7.6 Photon Cross-section for Aluminum.....	74
A.1 $T(u)$ for Typical Values of ρ	80

Acknowledgments

I would like to thank all those who donated their time and skill to make this experiment a success, particularly S. Ahmad, G. Beer, M. Dixit, J. MacDonald, G. Mason, P. Poffenberger, C. Sayre, and W. Sperry. I would like to give special thanks to A. Olin whose advice and willingness to discuss various aspects of the experiment proved most valuable. Thanks also to Peter Verstraaten for constructing the ^{13}C target. Finally, I would like to express my gratitude to my supervisor R.M. Pearce who provided excellent direction and advice, as well as much encouragement in this undertaking.

x

To my parents....

Chapter 1

Introduction

1.1 Exotic Atoms

Negatively charged heavy particles (pion: π^- or muon: μ^-) may bind with atomic nuclei to form what are called pionic or muonic atoms. The method of creating so called exotic atoms is to irradiate a target with a beam of π^- or μ^- . A particle from the beam is slowed down by electromagnetic interactions with atomic electrons surrounding the nucleus until it is eventually captured and pulled into an orbit around the nucleus. The energy level or binding energy E of the orbit is approximated by the Bohr formula:

$$E = -\mu(Z\alpha)^2/(2n^2) \quad \dots(1.1)$$

α is the fine structure constant, Z the charge of the nucleus, μ the reduced mass of the particle about the nucleus, and n the principal quantum number of the orbit. One may calculate the corresponding radius r :

$$r = (n^2/Z)(m/\mu)a_0 \quad \dots(1.2)$$

where m is the electron mass and $a_0 = .529 \times 10^{-8} \text{cm}$.

1.2 Pionic Atoms

Since the mass of a π^- is approximately 273 times that of an electron, the binding energy E for a given quantum number n is 273 times stronger than for electrons. Similarly, the Bohr radius is 273 times smaller. The radius of a pionic carbon

nucleus is about 2.5 fm ($1 \text{ fm} = 1 \times 10^{-13} \text{ cm}$), while the Bohr radius of the smallest pionic orbit is about 30 fm. The pion is believed to be captured by the atom near the first orbit with radius less than the innermost electron orbit. This corresponds to a principal quantum number $n=17$. The pion cascades from the initial capture level down to the ground state in about 10^{-15} s . This is short compared to the pion mean lifetime of $2.6 \times 10^{-8} \text{ s}$. During this cascade, X rays of energy equal to the difference in binding energies of each two sequential levels of the cascade are emitted.

The pion is a strongly interacting particle. The strong interaction between pion and nucleus invalidates the Bohr model for the lower n values. In the case of carbon, changes become detectable when the pion reaches the 2p level ($n=2$) and its wave function begins to overlap that of the nucleus. The binding energy of the 2p level is increased, in this case very slightly. Of the pions which reach the 2p level about 10% are absorbed by the nucleus directly from this level via the strong interaction, a small number undergo Auger transitions to the 1s level, and the majority undergo radiative transitions to the 1s level. The transition rates each contribute to the width of the 2p level. The radiative width is about .1 eV, the strong interaction width about 1 eV, and the Auger width is negligible.

Pions which reach the 1s level are quickly absorbed by the

nucleus. The rate of absorption from the 1s level is about three orders of magnitude higher than that from the 2p level. This is responsible for the Lorentz broadening of the 2p-1s X rays from pionic carbon. The strong interaction not only broadens the 1s level, but also decreases the binding energy, causing a net decrease in the energy of the X rays observed from the 2p-1s transition. In carbon the Lorentz broadening is about 3 keV and the decrease in binding energy about 6 keV.

As one progresses from carbon to heavier atoms, more pions are absorbed from the 2p level, hence decreasing the intensity of the 2p-1s transition. The 1s level Lorentz width increases as well. These two factors combine to prevent experimental observation of the 2p-1s transition for atoms with Z larger than about 12 where it is believed that virtually 100% of the pions reaching the 2p level are absorbed by the nucleus and never reach the 1s level. This effect serves to limit the energy of X rays observed in pionic atoms to no more than a few hundred keV since the transitions of highest energy are very much depleted by the strong interaction.

1.3 Experimentally Measured Quantities

Experimentally, one is interested in measuring the width Γ and energy E of a transition in a pionic atom. The width Γ of the 2p-1s transition is a measure of the rate of absorption of pions from the 1s level by the nucleus. It is possible to solve the Klein Gordon equation and to determine a form

of the optical potential necessary to produce the observed width Γ and energy E . [1]

The so-called strong interaction shift ϵ of the $2p-1s$ transition is the difference between the experimentally measured energy and the calculated energy obtained by solution of the Klein Gordon equation, including all effects except those due to the strong interaction.

Particularly valuable tests of theories of pionic atoms are measurements of the energies and widths of transitions in isotopic pairs. Such measurements have been performed on a variety of light atoms, the results of which are summarized in Table I. The effect of neutron deficiencies and excesses in these atoms is not well understood as yet.

Previous work (Table I) has measured the $2p-1s$ transition energy and width of pionic natural carbon. In this experiment a target of 99.7% pure ^{13}C was used to determine the energy and width of the $2p-1s$ X rays from $\pi^{13}\text{C}$ while a target of natural carbon (graphite) was used to acquire the data from which were extracted the values for $\pi^{12}\text{C}$.

[1] This method is applied numerically in the program PIATOM
M. Krell (1977)

Table I
 Measurements of Pionic 2p-1s Energies and Widths
 in Selected Isotopic Pairs

Isotope	Energy (keV)	Error (keV)	Width (keV)	Error (keV)	Reference
^1H	2.5	.1			Bailey, 1970
^2H	2.5928	+ .0016 - .002			Bailey, 1974
^3He	10.677	.003	.028	.007	Abela, 1979
	10.679	.004	.036	.007	Mason, 1980
^4He	10.6987	.002	.045	.003	Backenstoss, 1974
^6Li	24.192	.003	.195	.012	Backenstoss, 1973
^7Li	24.083	.004	.195	.013	Backenstoss, 1973
^{10}B	65.79	.11	1.68	.12	Harris, 1968
	65.902	.013	1.78	.03	Olin, 1980
^{11}B	65.00	.11	1.72	.15	Harris, 1968
	65.120	.026	1.72	.08	Olin, 1980
^{12}C	92.94	.15	2.96	.15	Backenstoss, 1967
	93.19	.12	3.25	.25	Harris, 1968
	93.3	.5	2.6	.5	Jenkins, 1966
	93.287	.043	2.66	.12	present work
^{13}C	92.227	.027	2.59	.11	present work
^{16}O	159.900	.090	7.92	.32	Schwanner, 1980
^{18}O	155.327	.105	6.62	.38	Schwanner, 1980

In Chapter 2 the experimental arrangement and data collection technique are described in detail. Chapter 3 deals with the method of analysis of the data. Chapter 4 discusses various calibrations which were performed as part of the analysis. Possible contamination of the $\pi^{13}\text{C}$ spectrum by $\pi^{12}\text{C}$ is discussed in Chapter 5. Chapter 6 presents results for the 2p-1s transition energies and widths in $\pi^{12}\text{C}$ and $\pi^{13}\text{C}$. Chapter 7 presents the determination of the 2p level widths, using relative intensity measurements, and 3d-2p transition energies for pionic ^{12}C and ^{13}C . Chapter 8 summarizes the results and conclusions reached.

Chapter 2

The Experimental Arrangement and Technique

2.1 The Beamline

The experiment was performed at TRIUMF, situated south of the University of British Columbia campus in Vancouver, B.C. The TRIUMF cyclotron delivered a beam of approximately 30 μA of 500 MeV/c protons down beamline 1, striking the production target (see Fig. 2.1). The secondary channel labelled M9, collects particles created in and around the production target at a backward angle of 45° from the direction of the proton beam, with an angular acceptance of about 30 milliradians. The channel was tuned to accept particles with momentum near 88 MeV/c (Fig. 2.4). The range of momenta accepted or momentum bite $\delta p/p$ is controlled by slits, which can be adjusted in the horizontal direction, located at the first dispersed focus approximately midway between the two bends. In this experiment the momentum bite was adjusted to 10%, to give a reasonable event rate at the target.

2.2 The Experimental Area

2.2.1 The Scintillator Telescope

The experiment was set-up at the second focus of the secondary channel M9, approximately 8.4 meters flight path from the production target (see Fig. 2.2). The scintillator telescope consisted of three plastic scintillators, labelled S_1 , S_2 , and S_3 . S_1 and S_2 were used to define the direction and

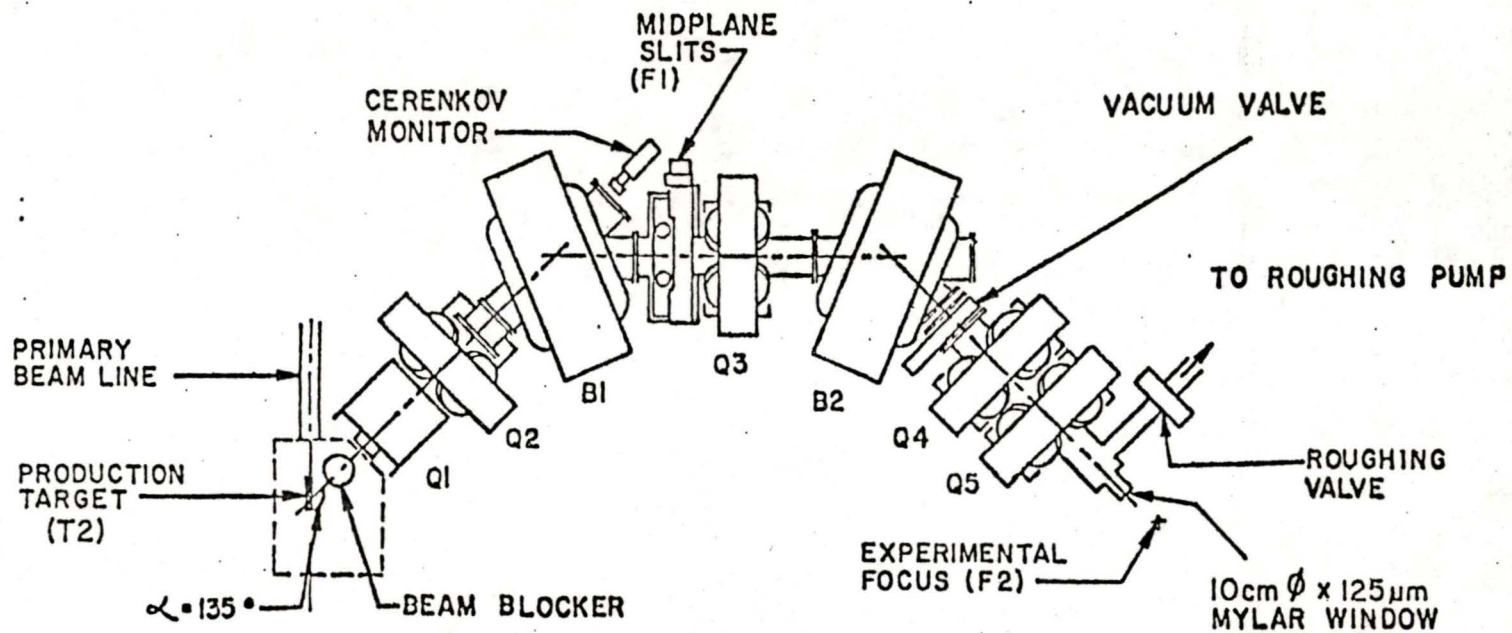


FIG. 2.1
 THE SECONDARY
 CHANNEL M9

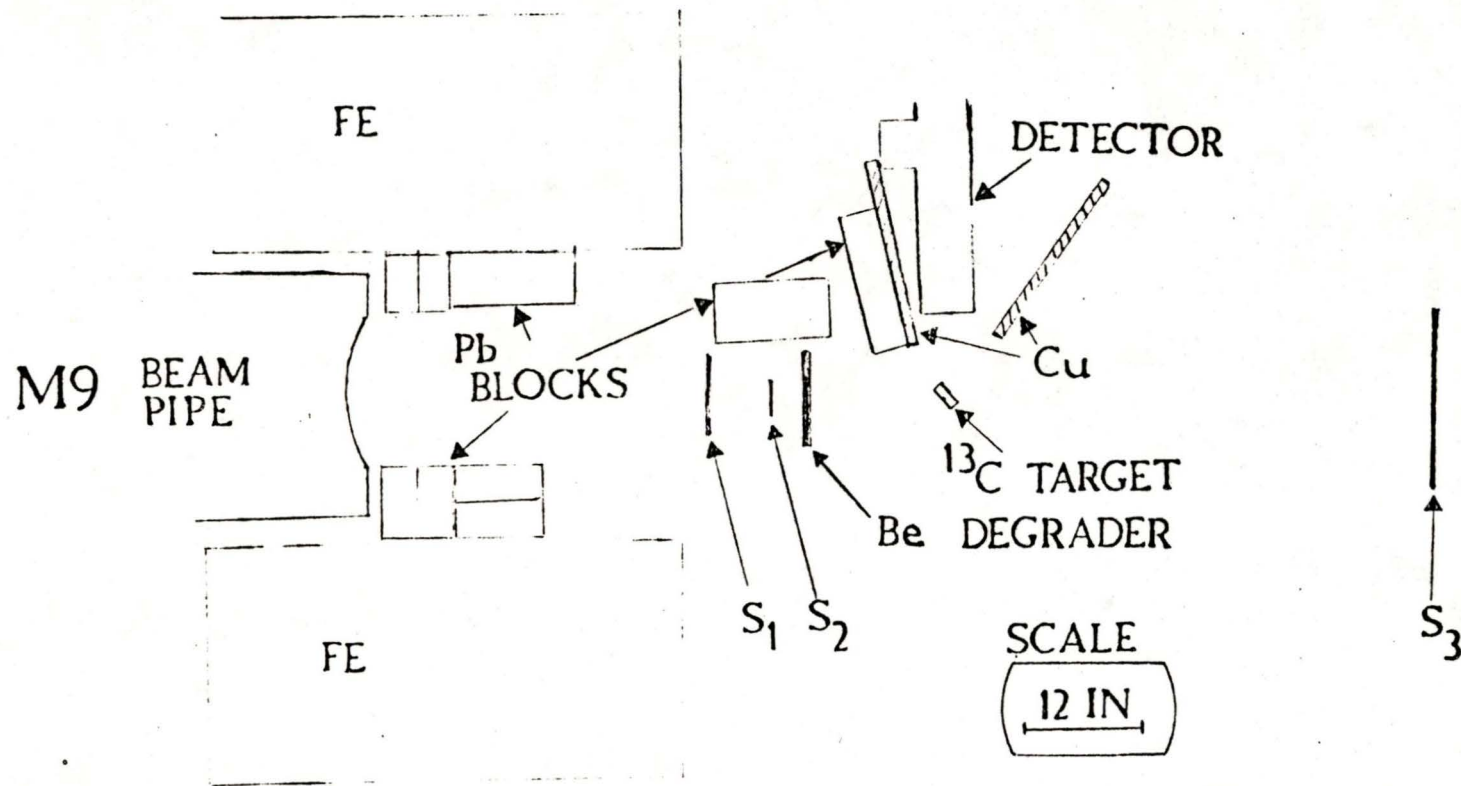


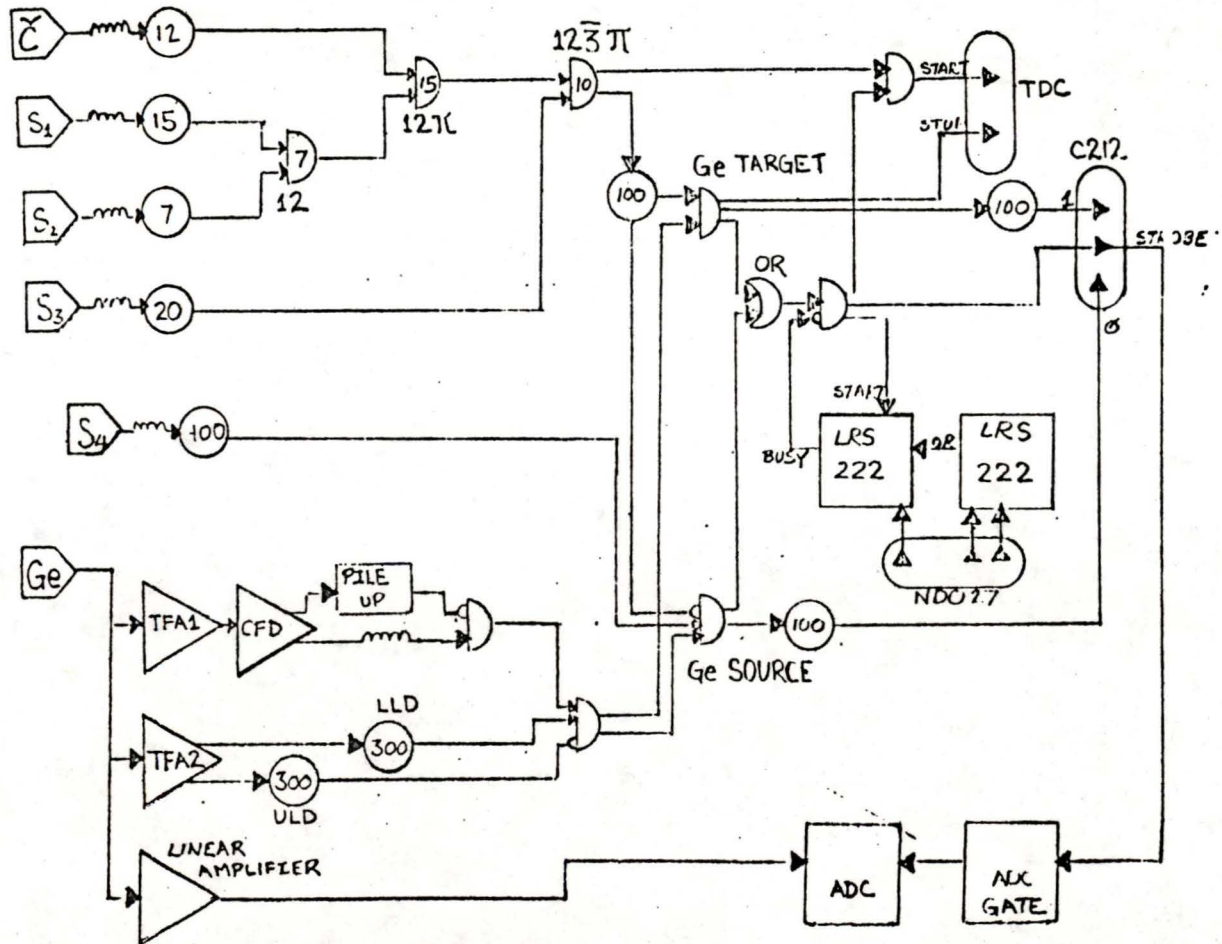
FIG. 2.2
THE EXPERIMENTAL AREA

size of the particle beam striking the target. This was done by requiring a "12" coincidence of counts from S_1 and S_2 due to a meson traversing both of the scintillators. Counter S_3 was much larger than the other two, being used to detect particles which passed through the first two scintillators but did not stop in the target, hence penetrating S_3 . S_3 was used to veto the 12 signal hence defining a stopped event (see Fig. 2.3). If the momentum of the particles is carefully selected most of the particles which stop will be pions, while the muons and electrons in the beam will pass completely through all scintillators. However there exists some probability that the particle will change direction, through scattering in the target, air, degrader, or scintillators, sufficiently to miss the veto counter S_3 and therefore be interpreted as a stopped event.

2.2.2 The Degradation and Range Adjustment for Pions

To adjust the range of the particles so that pions would stop in the target, rather than pass through S_3 , a beryllium degrader of 2 g/cm^2 thickness was placed immediately downstream from S_2 . Beryllium was chosen because stopping pions or muons do not produce X rays in the energy region being studied. Since the thickness of this degrader was not variable, fine adjustment was performed by variation of the channel momentum. A scintillator S_0 was used to simulate the ^{13}C target, placed at 45° to the beam, in the same position as the target. The number of stops in S_0 per "12" count was maximized by adju-

FIG. 2.3 LOGIC DIAGRAM



ting the channel momentum (Fig. 2.4). The maximum value of this ratio was found to occur at a momentum of 88 MeV/c.

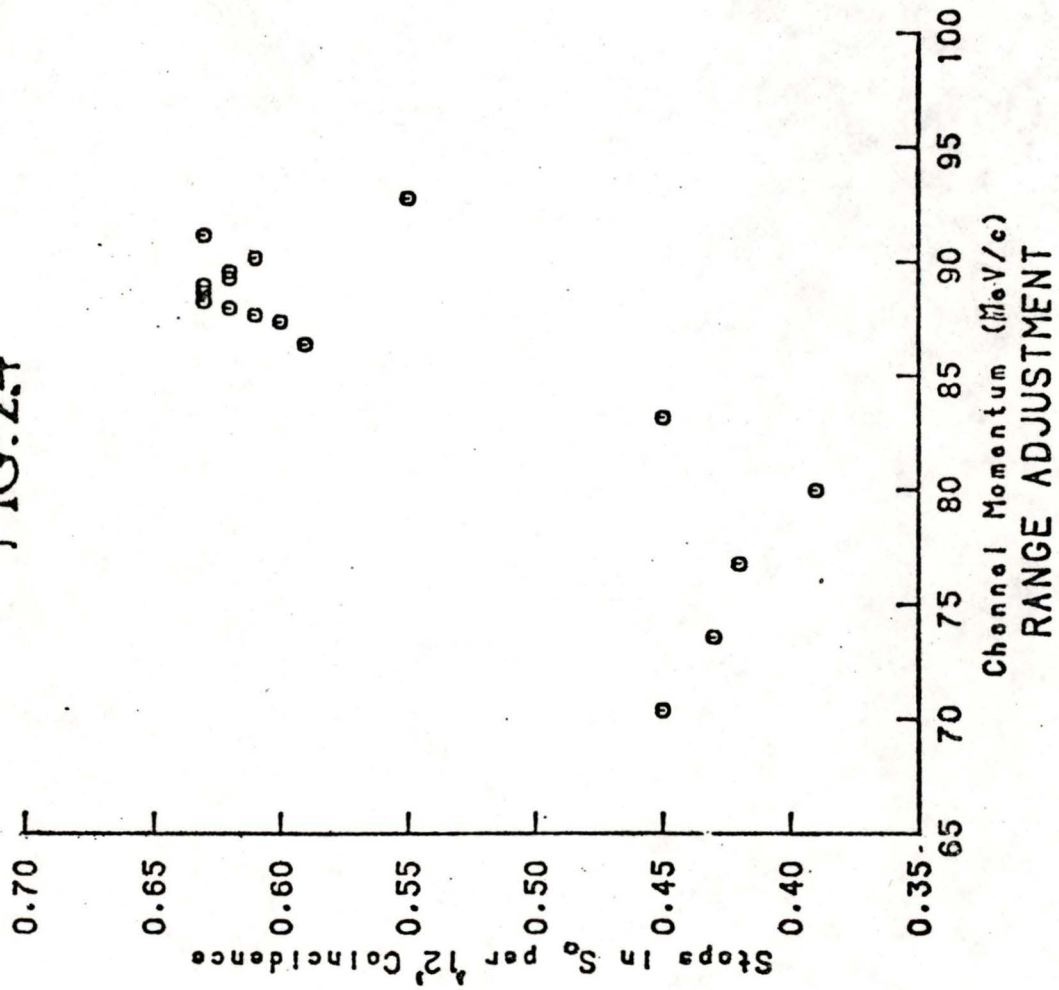
2.2.3 The Targets

Three targets were used in this experiment. The ^{13}C target is shown in Fig. 2.5. It consists of 6.76 g of powdered carbon (99.7% ^{13}C and .3% ^{12}C) held by an aluminum cylindrical case made from .003 inch foil. An empty duplicate of this casing was used as the target in the target-empty run. The ^{12}C target was a slab of natural graphite, approximately 1/4 inch thick. All three targets were placed at 45° to the direction of the beam.

2.2.4 Shielding

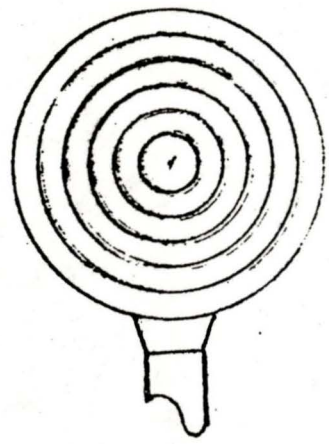
It was necessary not only to shield the detector from the beam, but also from non-target sources of pionic X rays: in particular from the natural carbon in certain of the scintillators. For this reason it was not possible to use the normal set up in which a thin counter S_1 is close to the target and defines the extent of the beam striking the target much more rigorously, since stops in S_1 could not be distinguished from stops in the target using a $123\bar{4}$ arrangement. S_2 was placed well upstream of the target in order that it could be well shielded from the detector. Also since stops in the upstream insensitive layer of S_3 are indistinguishable from target stops, veto counter S_3 was moved further downstream from the target than is usual in order that it could be shielded from the detector

FIG. 2.4



THE ^{13}C TARGET

FRONT
VIEW



SIDE
VIEW



SCALE: 1 in

MATERIAL: .003 in. AL

FIG. 2.5

with a 1/2 inch copper sheet (see Fig. 2.2).

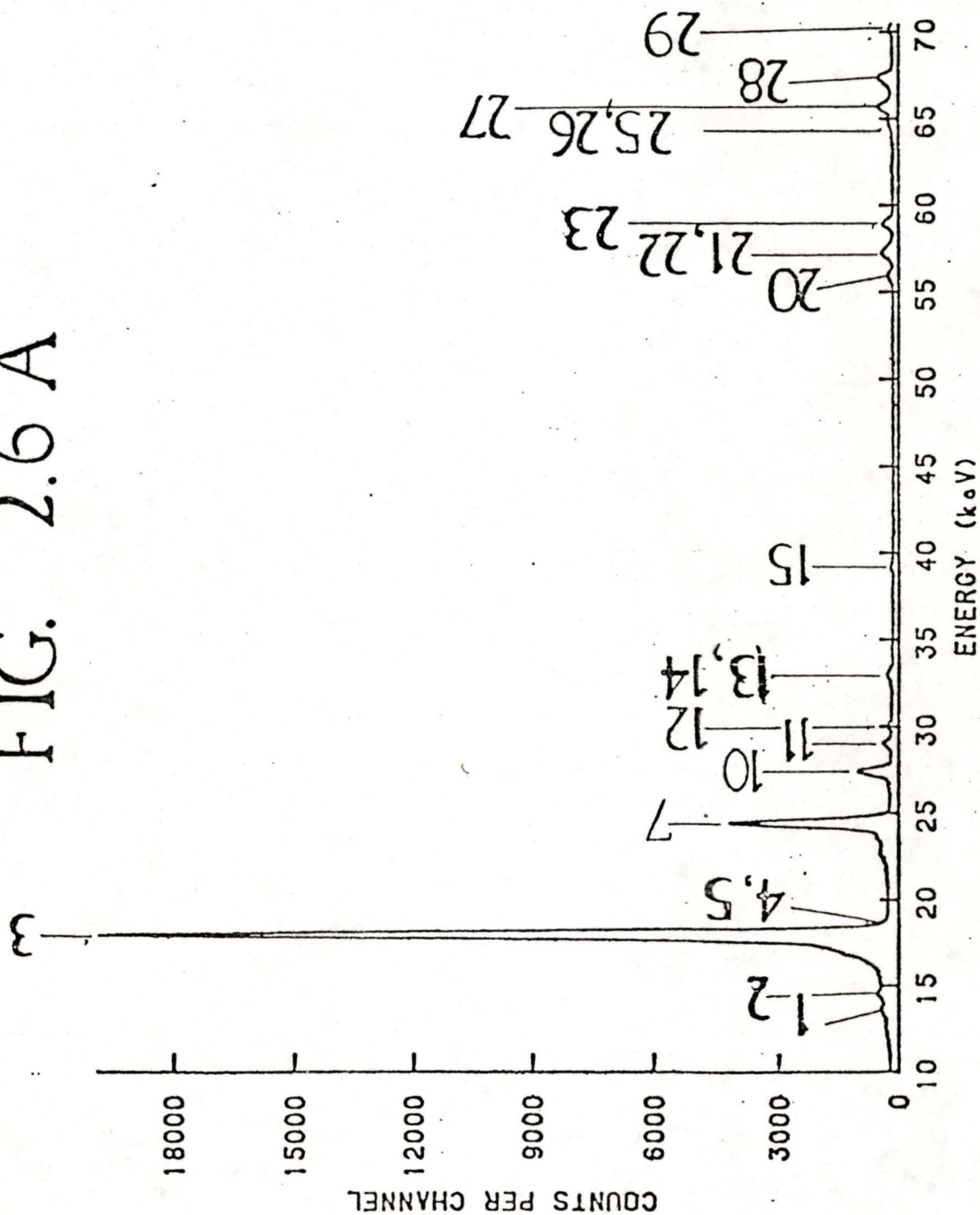
To reduce nuclear γ rays and electronic X rays from the lead shielding a 3/8 inch copper sheet was used. The effectiveness of this arrangement is borne out by the analysis in Chapter 5 which shows that the $\pi^{12}\text{C}$ X ray contamination of the ^{13}C spectrum is less than .6% the intensity from the ^{13}C target. Weak chlorine peaks were observed from the black tape covering the scintillators as well as copper peaks from the shielding, and nitrogen and oxygen peaks from air (see Fig. 2.6 a,b, 2.7 a,b, and 2.8 a,b). Peaks from the beryllium degrader were not observed.

2.3 The Detection System

2.3.1 Time of Flight Separation

Secondary particles are produced in bunches at the production target every 43 ns, corresponding to the 23 MHz operating frequency of the cyclotron. Since the particles in a bunch have the same momentum but different masses, structure arises as the particles travel down the channel. Pions, being the heaviest, begin to lag behind the muons, and the muons behind the electrons. By the time they reach the experimental area, the three distributions of flight times are clearly resolved at a momentum of 88 MeV/c. This makes possible the selection of particles likely to be pions by time-of-flight. A probe detects the arrival of a bunch of protons at the production target, generating a signal which is compared to the "12" coincidence signal, to form a timed 12 π

FIG. 2.6 A



The Pionic 12 C Spectrum

FIG. 2.6 B

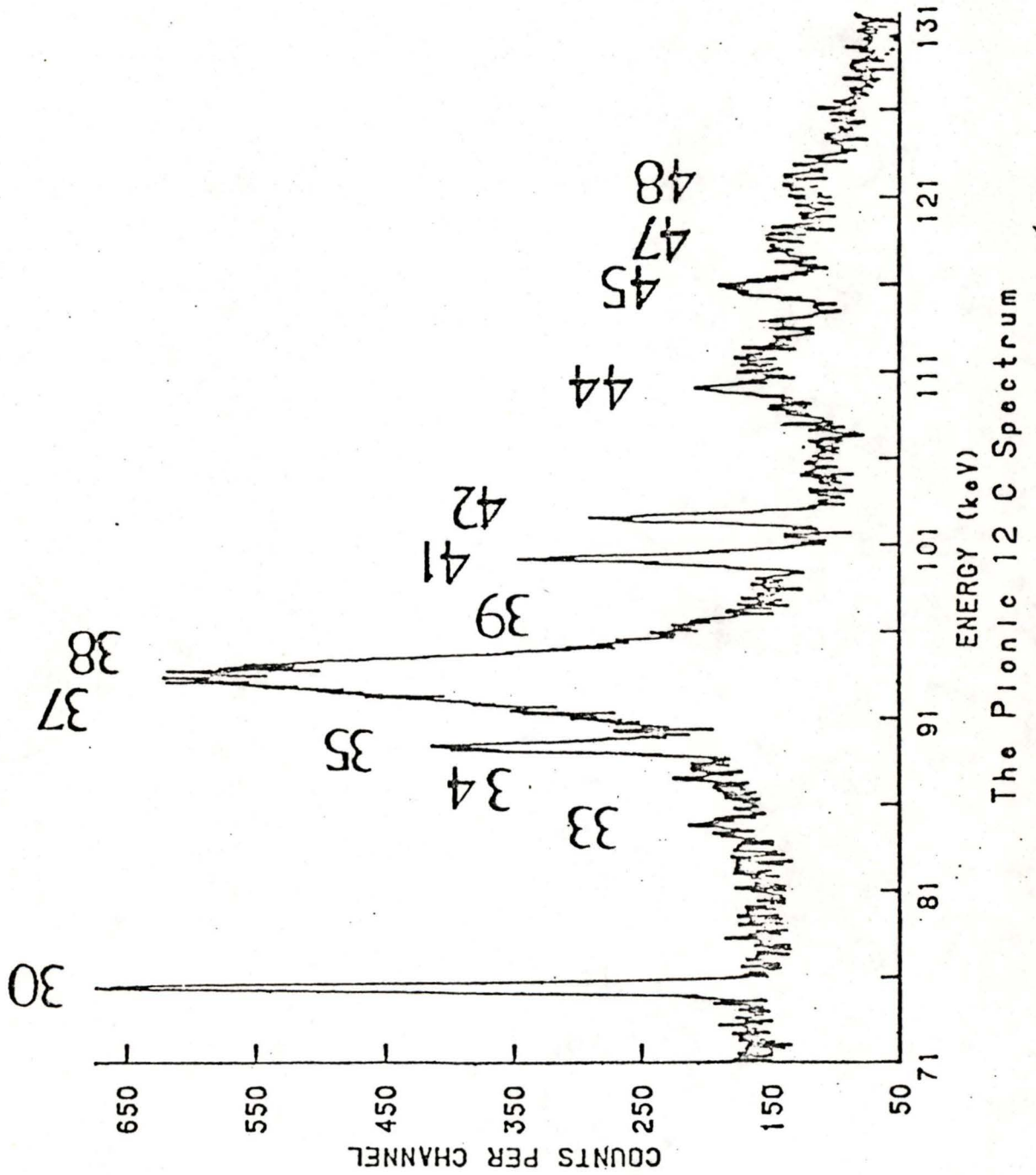
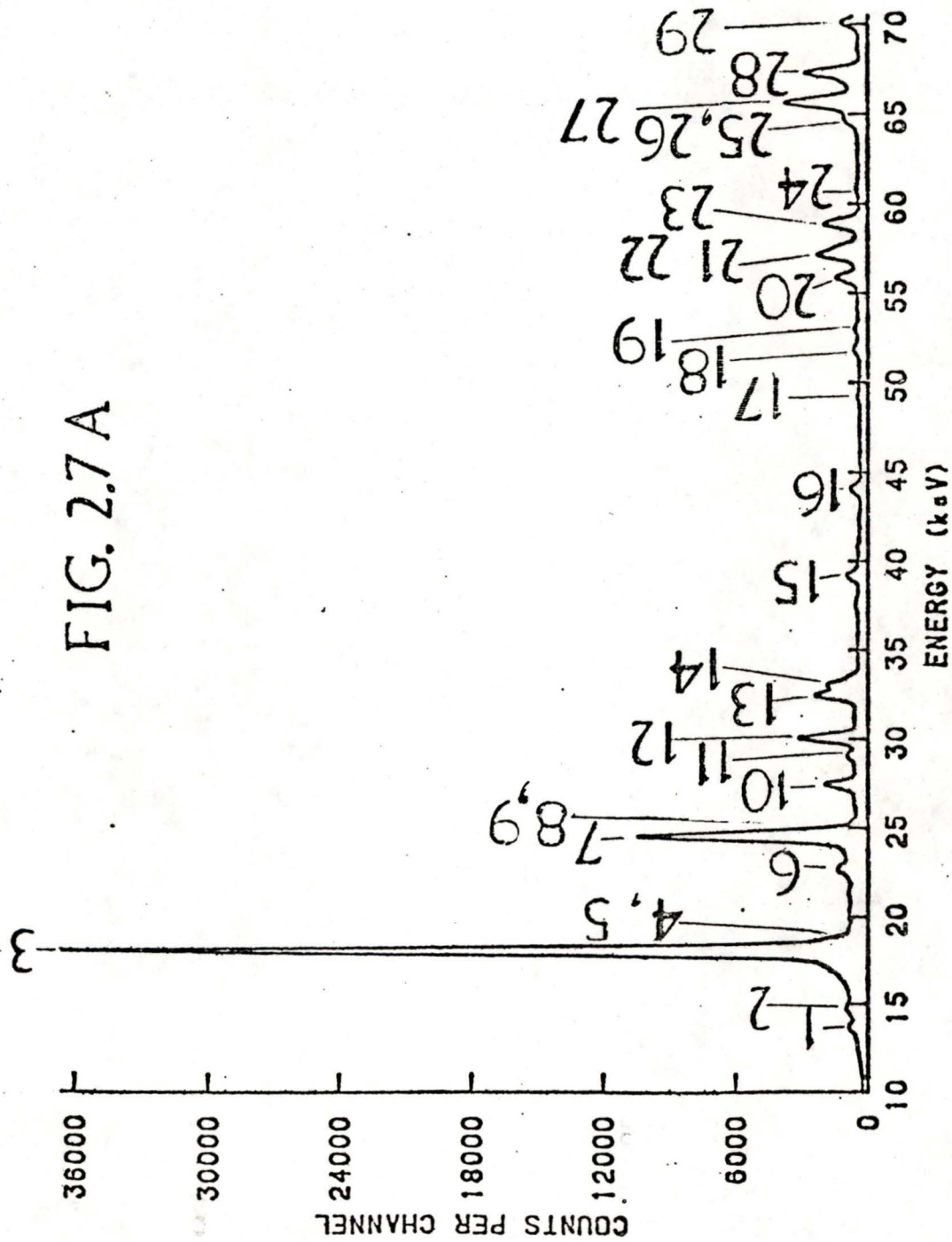
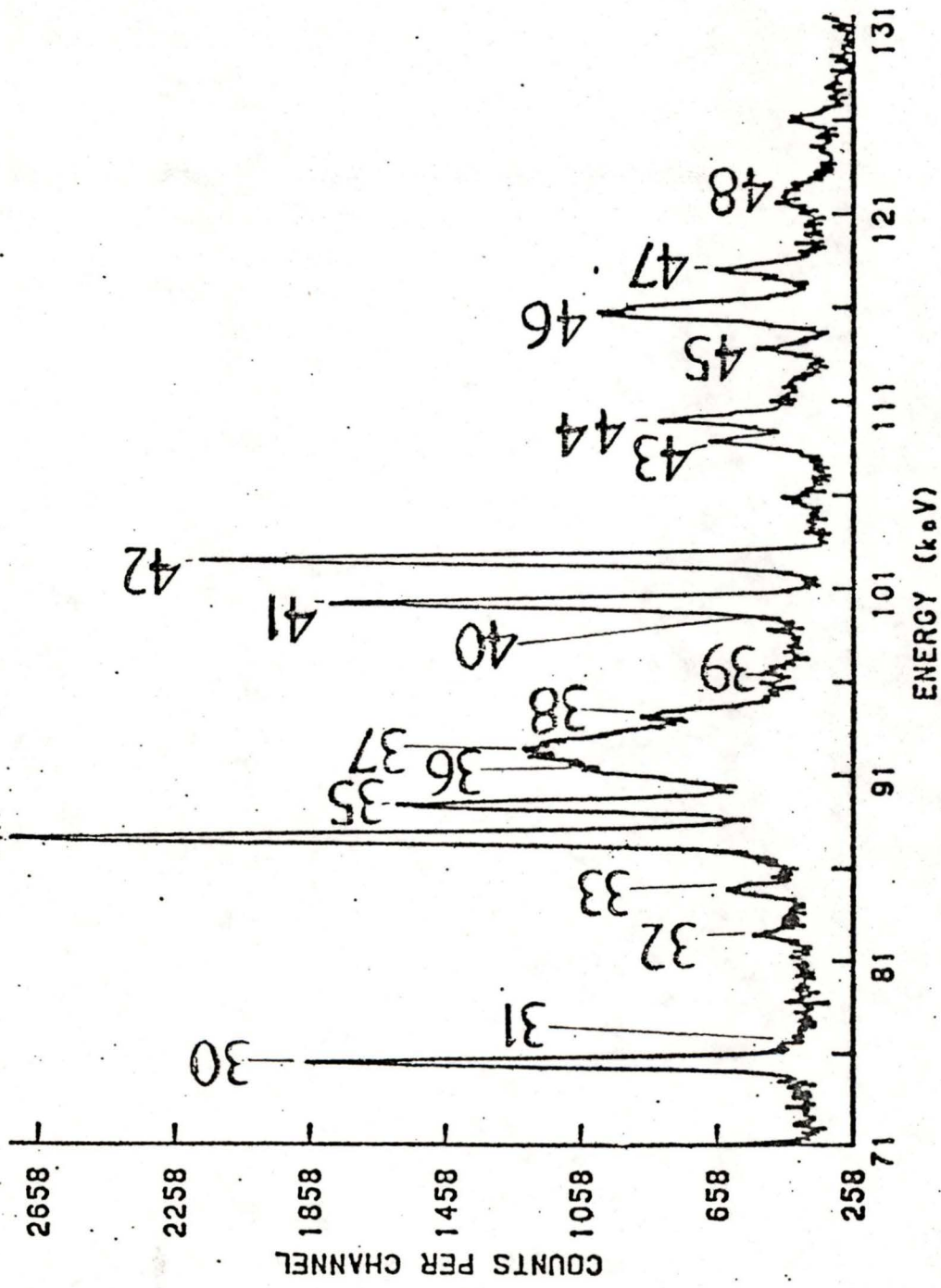


FIG. 2.7 A



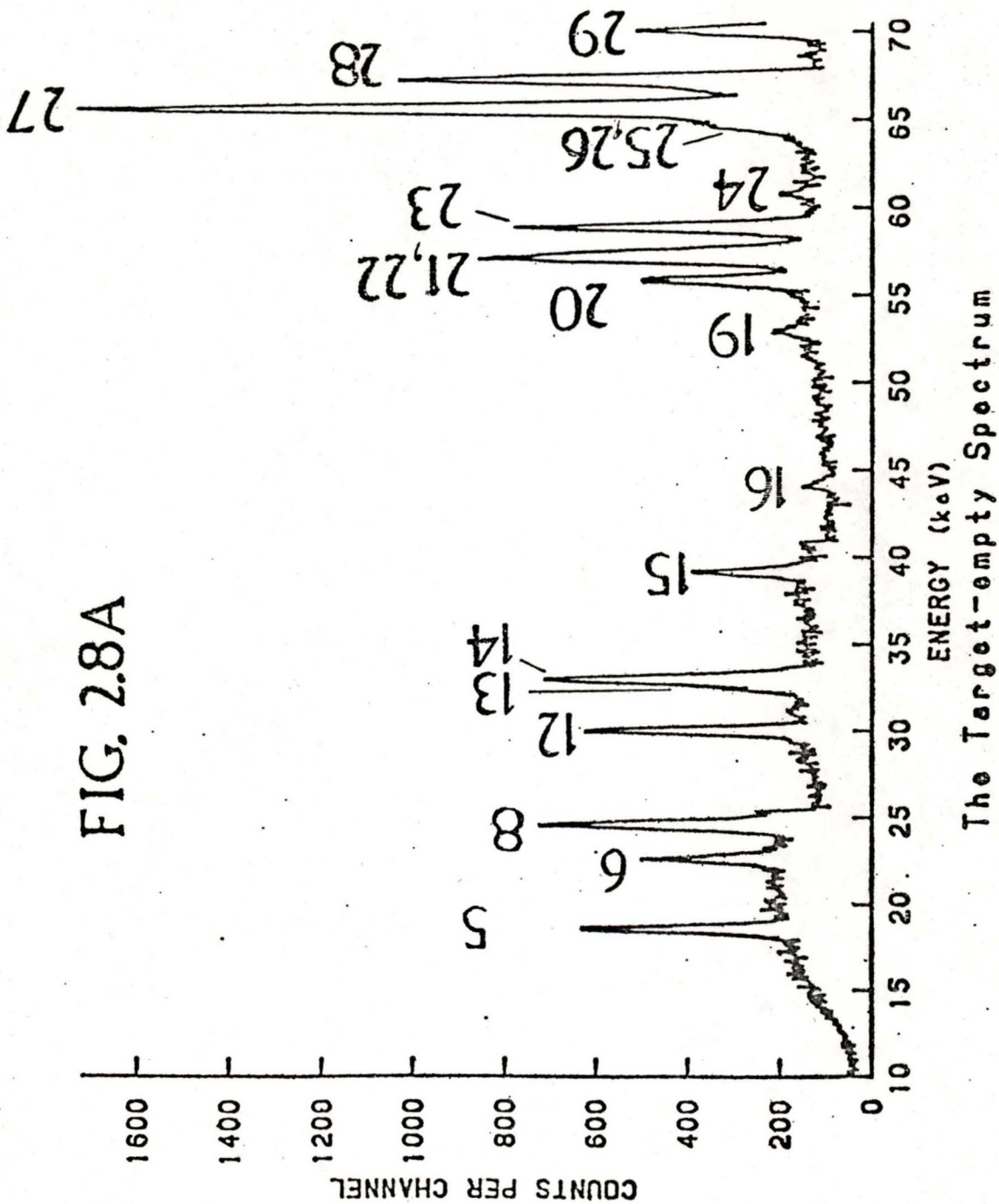
The Pionic ^{13}C Spectrum

FIG. 2.7B



The Pionic ¹³C Spectrum

FIG. 2.8A



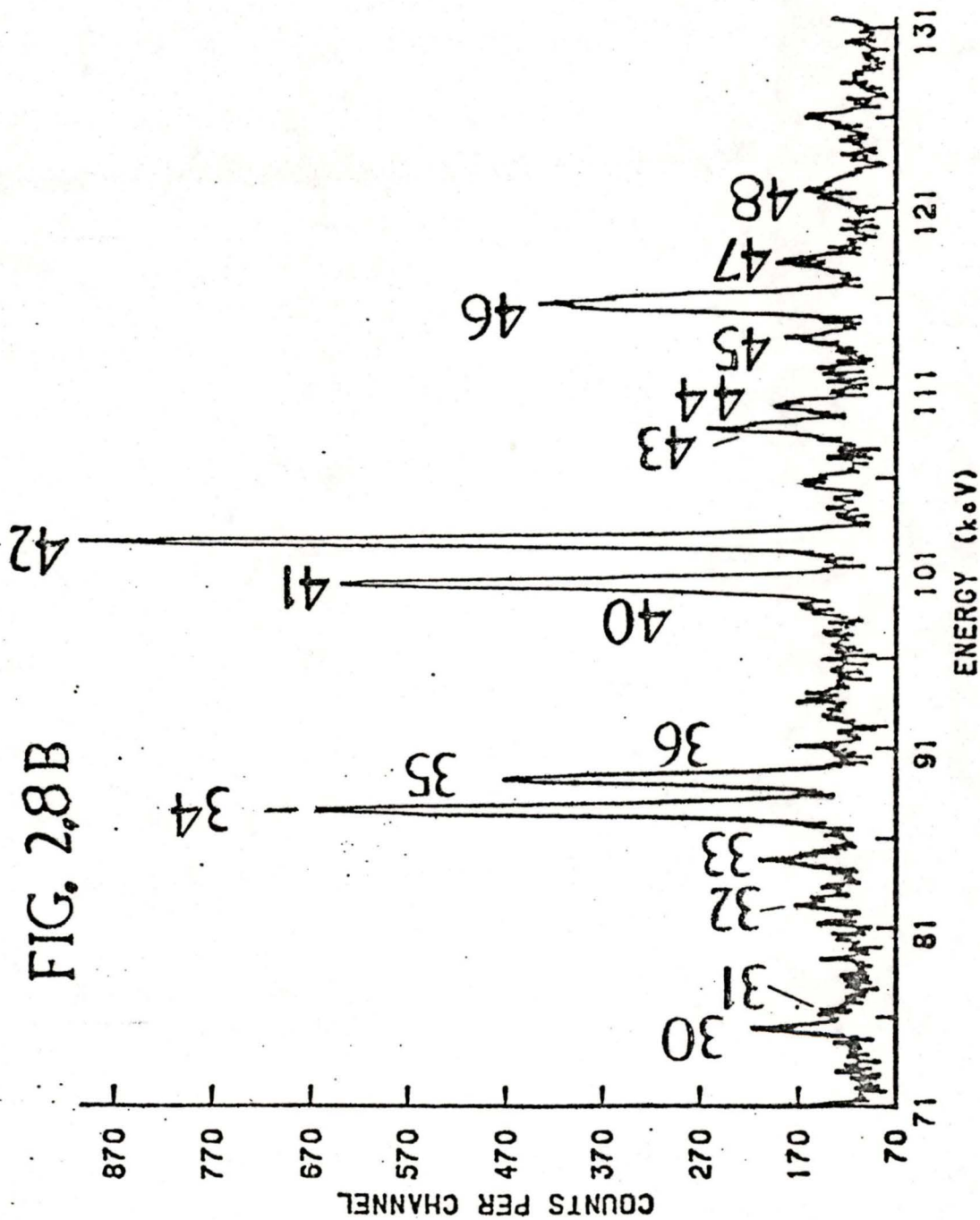


FIG. 2.8B

The Target-empty Spectrum

COUNTS PER CHANNEL

ENERGY (keV)

Table IIKey to Peak Identities in Figures 2.6, 2.7, and 2.8

1 μC 3-2	24 πCu 7-5
2 πCu 8-7	25 Ta $K\beta_2$
3 πC 3d-2p	26 Ta $K\beta_1$
4 μC 4-2	27 μAl 3-2 and $\gamma^{182}\text{Ta}$
5 μN 3-2	28 $\gamma^{182}\text{Ta}$
6 πCu 7-6 and μAl 4-3	29 πCu 5-4
7 πC 4f-2p	30 μC 2-1
8 πN 3-2 and μO 3-2	31 πCl 5-3
9 μN 4-2	32 μCu 6-4
10 πC 5g-2p	33 $\gamma^{182}\text{Ta}$
11 πC 6h-2p	34 πAl 3-2
12 πAl 4-3	35 μC 3-1 and μAl 4-2
13 πO 3-2	36 $\gamma^{23}\text{Na}$
14 πN 4-2	37 πC 2p-1s
15 πCu 6-5	38 μC 4-1
16 πO 4-2	39 μC 5-1
17 πO 5-2	40 μCu 5-4 and μAl 5-2
18 πCl 4-3 and πAl 6-3	41 $\gamma^{182}\text{Ta}$
19 μCu 5-4	42 μN 2-1
20 Ta $K\alpha_2$	43 πCu 6-4
21 Ta $K\alpha_1$	44 $\gamma^{19}\text{F}$ and πC 3-1
22 W $K\alpha_2$	45 $\gamma^{182}\text{Ta}$ and μCl 3-2
23 W $K\alpha_1$	46 $\gamma^{182}\text{Ta}$ and μCu 4-3

Table II (continued)47 μ Al 4-248 μ N 2-1 and μ N 3-1

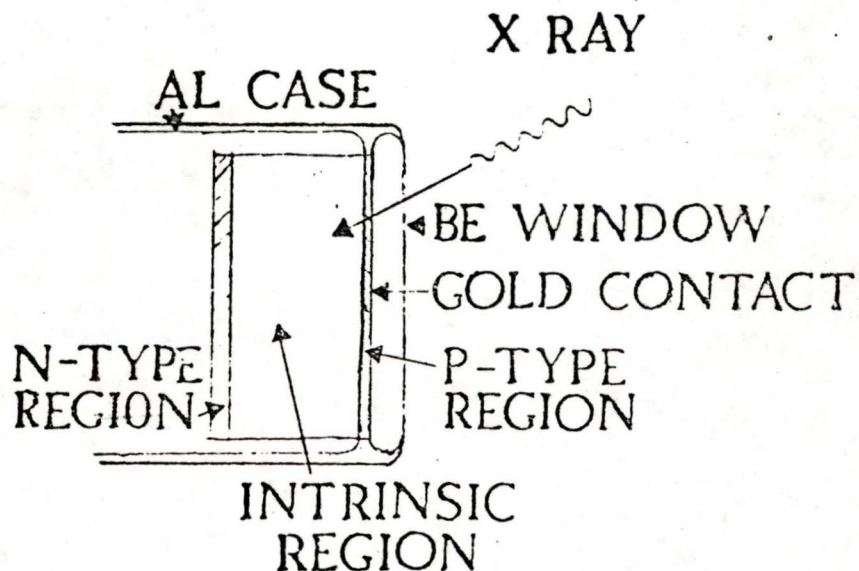
signal (see Fig. 2.3).

2.3.2 The Detector and Accompanying Electronics

An Ortec hyperpure germanium solid state detector, cooled to liquid nitrogen temperature was used. The in-beam resolution of the detection system was 560 ± 20 eV at 90 keV (see Sections 3.1.1 and 4.3.1). A schematic of a Ge detector is shown in figure 2.9. The efficiency (see Section 4.2) was a maximum near 50 keV, falling by about 50% at 90 keV.

Fig. 2.9

Schematic of a Ge Detector



Photons incident on the Ge crystal produce ionization, proportional to their energy, which is collected by the detector. The detector pre-amplifier, cooled to reduce electronic "shot" noise, produces a pulse with maximum voltage proportional to the charge collected.

The pre-amp signal is fed to a linear amplifier which smooths and amplifies the pulse before passing it to an analog-to-digital converter (ADC) which outputs the desired channel number (0-4095) corresponding to the voltage of the pulse received. However, the ADC performs the conversion only if a certain gate is received at the same time to indicate that the pulse is suitable for histogramming.

In addition to treating the analog signal, there are some fast logic signals which are used to perform the following functions:

- (i) to route the X ray and calibration peaks into different spectra, being careful to process them in the same way (see Chapter 4).
- (ii) to discard pulses outside the dynamic range of interest.
- (iii) to discard piled-up pulses.

The pre-amp pulse is fed through a timing filter amplifier (TFA1, Fig. 2.3), which differentiates the pulse and then through a constant fraction discriminator (CFD), which gives a fast pulse to the pileup gate whenever a photon is

detected. The pileup gate is used to veto the analysis of any pulses which overlap and consequently do not have the correct energy.

The pre-amp pulse is also fed through TFA2 to perform upper and lower level discrimination and thus prevent the unnecessary analysis of pulses with energy either too high or too low to be of interest. The pulses which are of the correct energy and are not piled up form the "clean Ge" coincidence signal.

If a "clean Ge" signal occurs within a 100 ns interval of a π -stop event, in addition to signalling to the computer that there is a pion event to be histogrammed, a time-to-digital converter (TDC) is started. The starting time depends on the timing of the "clean Ge" pulse since the π -stop signal used here is widened to 100 ns. The TDC is stopped by a narrow π -stop pulse. If, on the other hand, no π -stop event has occurred and scintillator S₄ has registered a count in the last 43 ns the "clean Ge" pulse signals to the computer that the event is to be histogrammed in the source (calibration) spectrum.

2.3.3 The Computerized Data Acquisition System

A NOVA mini-computer was used to monitor and histogram the data on disk, using the program PHA (J. Kulkula). The maximum event rate which can be handled by this system is on the order of 1000 events per second. The NOVA was interfaced to the experiment using the CAMAC system. Each event (called a LAM: "look-at-me") received by the computer

(C212 strobe, Fig. 2.3) caused the computer to read the C212 word (bits 1 and 0) which indicated whether the event was associated with the target or the calibration source. If the LAM was associated with the target, the TDC was also read and, depending upon a set of previously defined limits for various ranges of channel numbers, the event was histogrammed either in the prompt pion spectrum or the delayed pion spectrum. If the LAM was associated with the source, it was histogrammed in the calibration spectrum.

Chapter 3

The Fitting Process

3.1 Lineshape

The fitting program employed was a modified version of the least squares FORTRAN code JAGSPOT (Olin 1978) [1]. The program was used to fit peaks using lineshapes described below.

3.1.1 Gaussian

This kind of peak results from detection of a class of photons whose energies are distributed as a δ function, of width much smaller than the detector resolution, about a central value E_0 . The energy of the peak is defined by the energy of the δ function and is identical to the energy at which the Gaussian takes on its maximum amplitude γ . The assumed lineshape fit to the data is then:

$$f(x_k) = \gamma \exp[-(x_k - x_0)^2 / (2\sigma^2)] \quad \dots(3.1)$$

where x_0 is the position of the peak and σ the standard deviation of the Gaussian distribution. Tailing in the response function is considered as part of the background (section 3.1.3). The area of the peak is just the total area of the Gaussian.

3.1.2 Lorentzian

The Lorentzian shape results from detection of a class of photons whose energies are distributed about a central value

[1] Modifications are discussed in Appendix C.

E_0 continuously according the probability law:

$$P[E] \propto (\Gamma^2 + (E - E_0)^2)^{-1} \quad \dots(3.2)$$

where Γ is the Lorentzian full width at half maximum. As was the case in 3.1.1 above the analytic convolution of the Lorentzian shape and the detector response function is fit to the data. The form of the lineshape is then (Olin, 1978):

$$f(x_k) = \gamma \frac{2\pi}{\Gamma} \operatorname{Re} \omega \left(\frac{x_0 - x_k}{2^{1/2}\sigma} + \frac{\Gamma/2}{2^{1/2}\sigma} \right) \quad \dots(3.3)$$

where ω is the complex error function and $4\gamma/\Gamma^2$ the amplitude of the peak. Such peaks may be shown to have area (Olin 1978):

$$\gamma(2\pi)^{3/2}\sigma/\Gamma \quad \dots(3.4)$$

In terms of the more usual FWHM of the detector response function, 3.4 becomes:

$$\frac{\gamma\pi^{3/2}\text{FWHM}}{\Gamma \ln^{1/2}(2)} \quad \dots(3.5)$$

3.1.3 Background

The background fit to the data consisted of two parts. The first was a standard background, the intensity of which was made to vary linearly with energy. The second part consisted of low energy exponential tailing or tails of all non-background parts of the fit. The form of the background is then:

$$b(x_k) = a_1 + a_2 x_k + T_k \quad \dots(3.6)$$

where a_1 and a_2 are constants to be determined and T_k is the

additional background due to tailing of the detector response function ^[1].

3.1.4 Efficiency

The relative efficiency was determined from fits of the source spectra (see Section 4.2). In the fitting process the correction $\epsilon(x)$, called the efficiency function, was applied only to Lorentzian peaks, since these peaks, unlike others, consist of photons whose energies vary over a range before detection. Since efficiency is not expected to affect the detector response function no correction was applied to either Gaussian peaks or to the tailing of the response function. The linear part of the background is assumed to be generated by processes separate from those which determine $\epsilon(x)$ and hence not influenced by efficiency considerations, however it is possible that fits of large regions may benefit from modification of the linear background by $\epsilon(x)$ since the intensity of the background is in part due to contributions from weak peaks, and is therefore influenced by efficiency considerations.

3.2 The Best Fit Criterion

The least squares fit to the data is performed iteratively to seek a minimum in the random variable χ^2 .

^[1] See Appendix A.

Since the counts in each channel are assumed to be Poisson distributed, seeking a minimum in χ^2 corresponds to seeking the fit of maximum likelihood. The fitting functions discussed in 3.1 above are non-linear, and although the iteration method (Marquardt-Levinson) employed guarantees convergence to a local minimum in χ^2 , it does not guarantee that smaller minima do not exist, nor the uniqueness of any such minima. It is necessary to perform many fits, allowing different free parameters and giving different starting values before one can be reasonably sure that the "best fit" has been found. The means of comparing such fits is to use the value of $\chi^2/(n-m)$ as a measure of the "goodness of fit", where n is the number of data points in the fit and m the number of free parameters in the fitting function. A minimum in $\chi^2/(n-m)$ indicates the best fit to the data.

Chapter 4

Calibration

Calibration spectra of ^{182}Ta were acquired under the same instantaneous beam rate as the pionic spectra ^[1]. This was done by requiring a count in the scintillator labeled S_0 ^[2], situated near the beam but not in the pion telescope formed by the other three scintillators S_1 , S_2 , and S_3 . Such a count initiated a logical gate of up to 100 ns duration in which any X rays detected by the Ge detector were classified as "source" counts and consequently histogrammed by the computer in the source or calibration spectrum instead of in the pion spectrum. If a π -stop signal were received within the 100 ns interval, the gate indicating source counts was terminated prematurely and the gate indicating pion counts initiated.

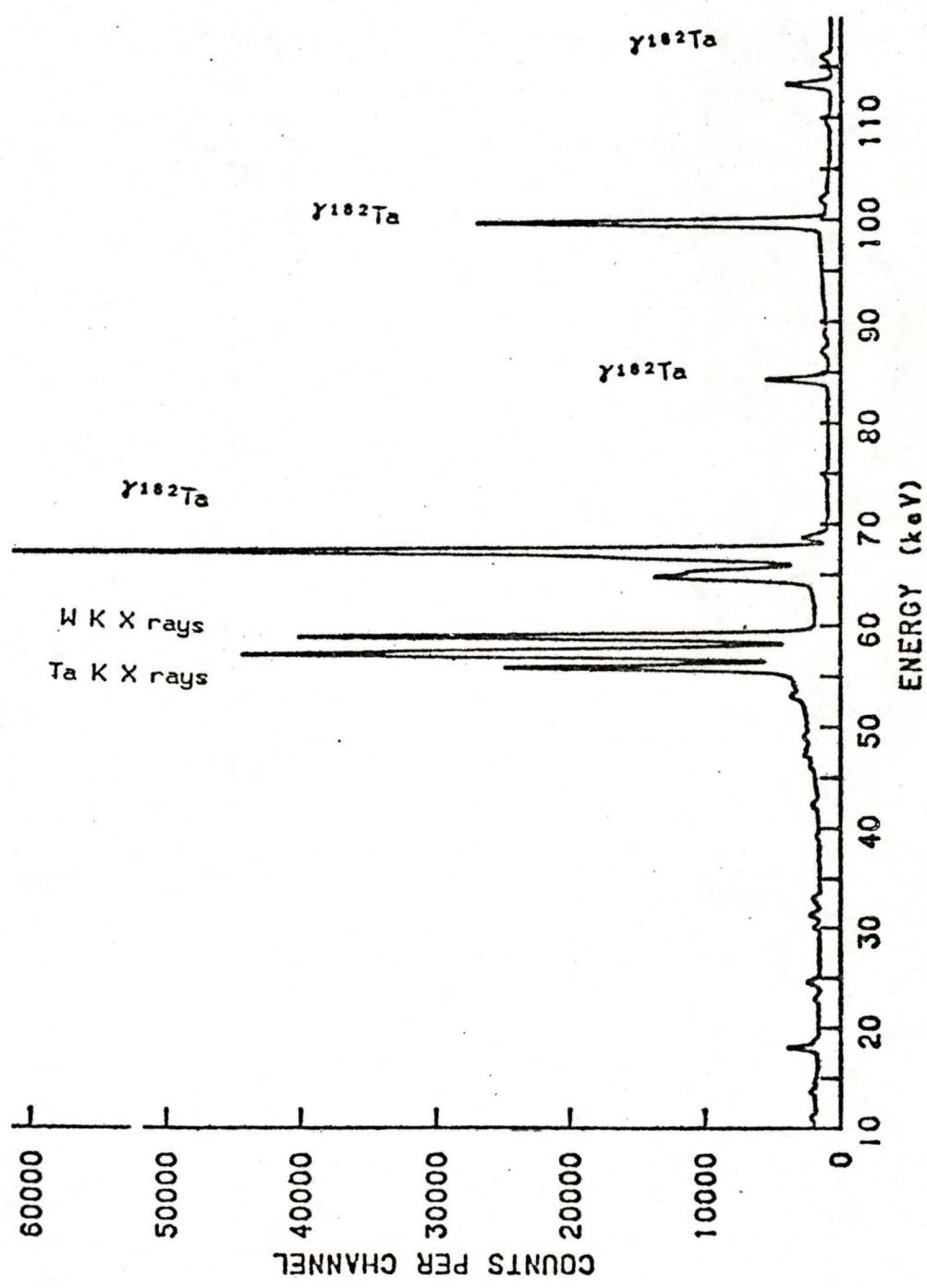
The calibration spectra thus obtained contained Gaussian peaks due to detection of X rays and γ rays from the decay of radioactive ^{182}Ta , as well as weak muonic and pionic X rays. Two additional calibration spectra were acquired without beam using pairs of sources: one using ^{57}Co and ^{182}Ta , the other using ^{241}Am and ^{182}Ta ^[3]. Peaks in all of the above calibration spectra were fit to Gaussians with low energy ex-

[1] See Fig. 4.1 a,b and 4.2 a,b.

[2] See Fig. 2.2.

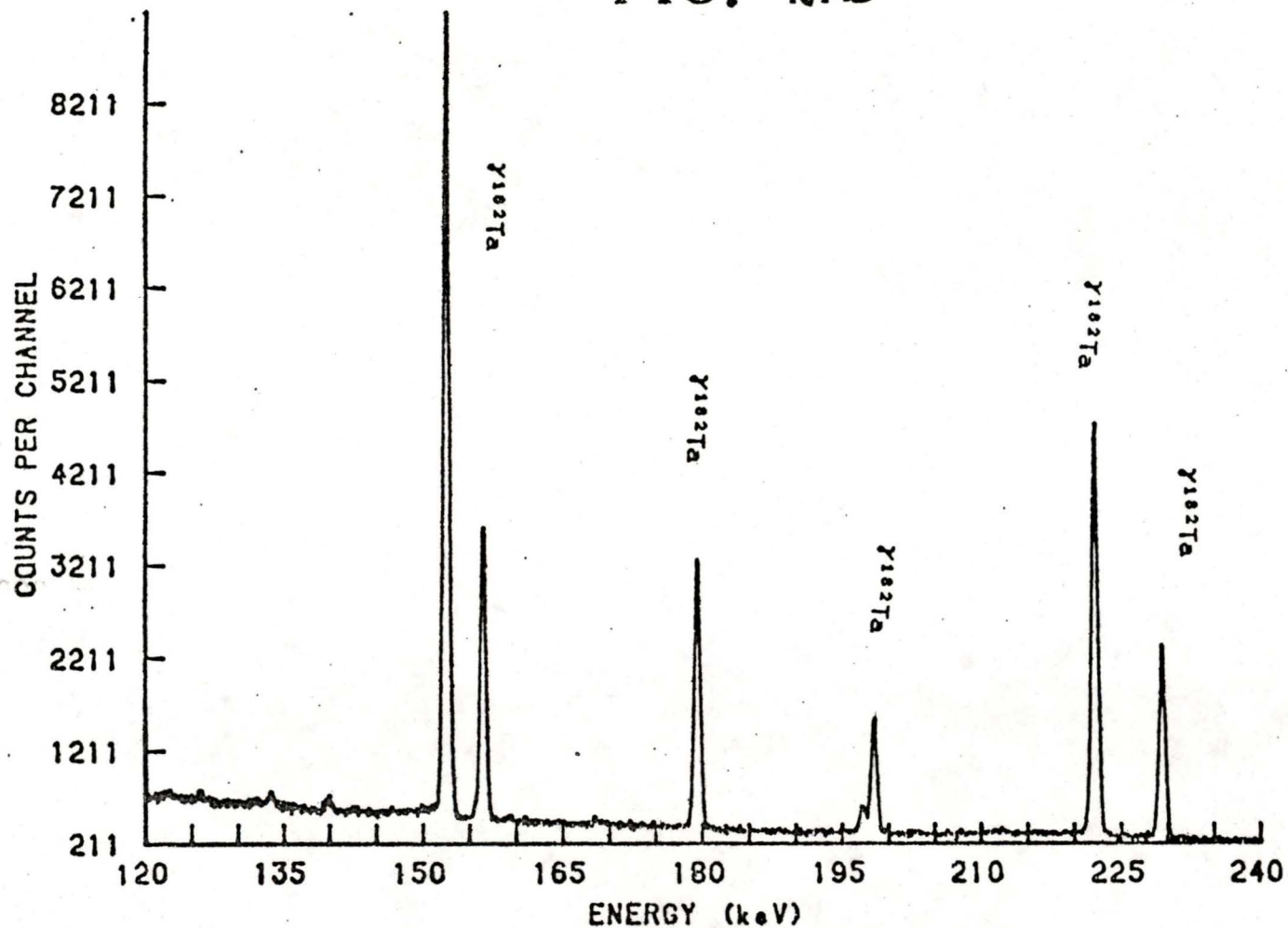
[3] See Fig. 4.3 a,b and 4.4 a,b.

FIG. 4.1A



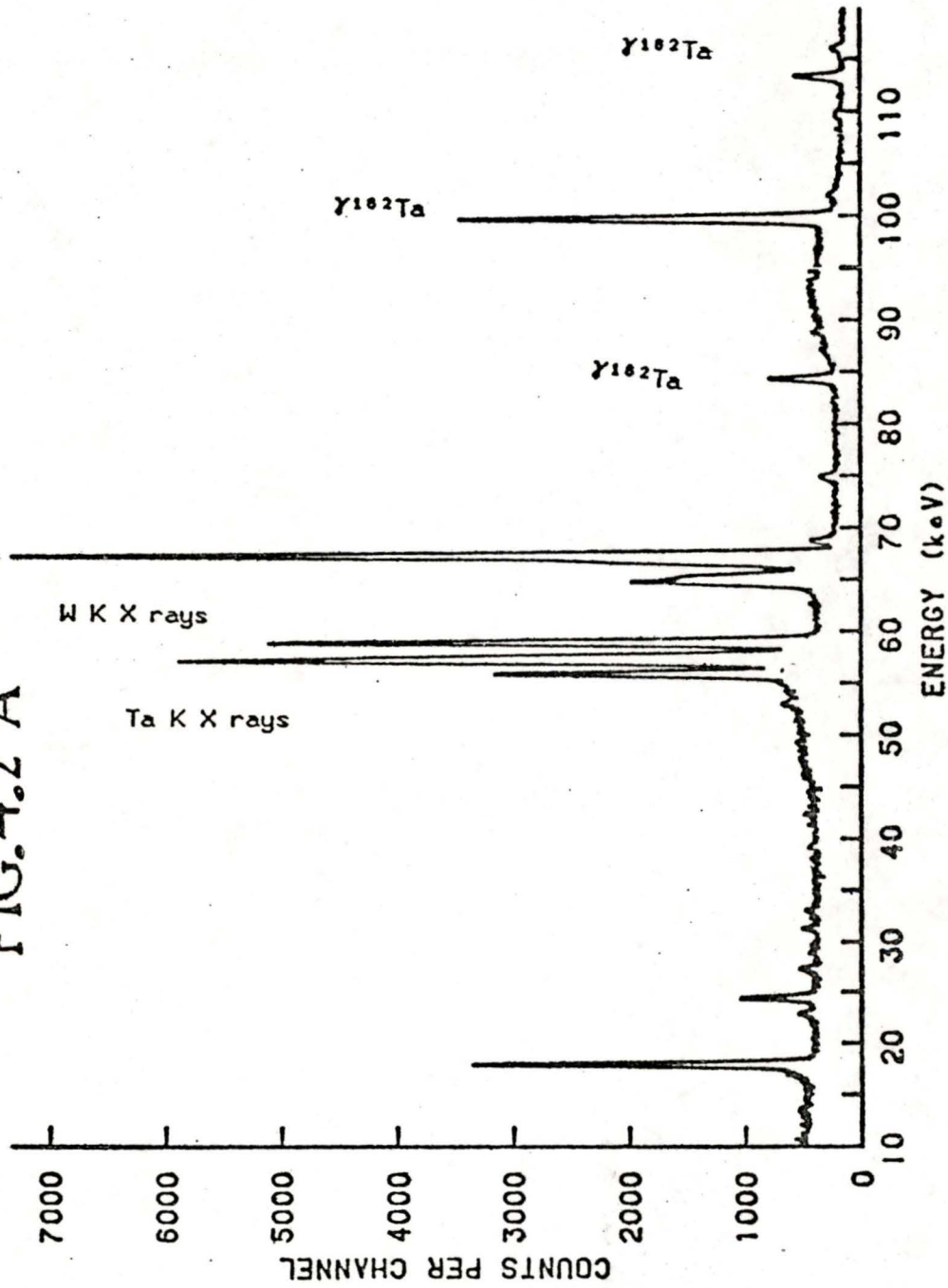
THE ^{13}C CALIBRATION SPECTRUM

FIG. 4.1B



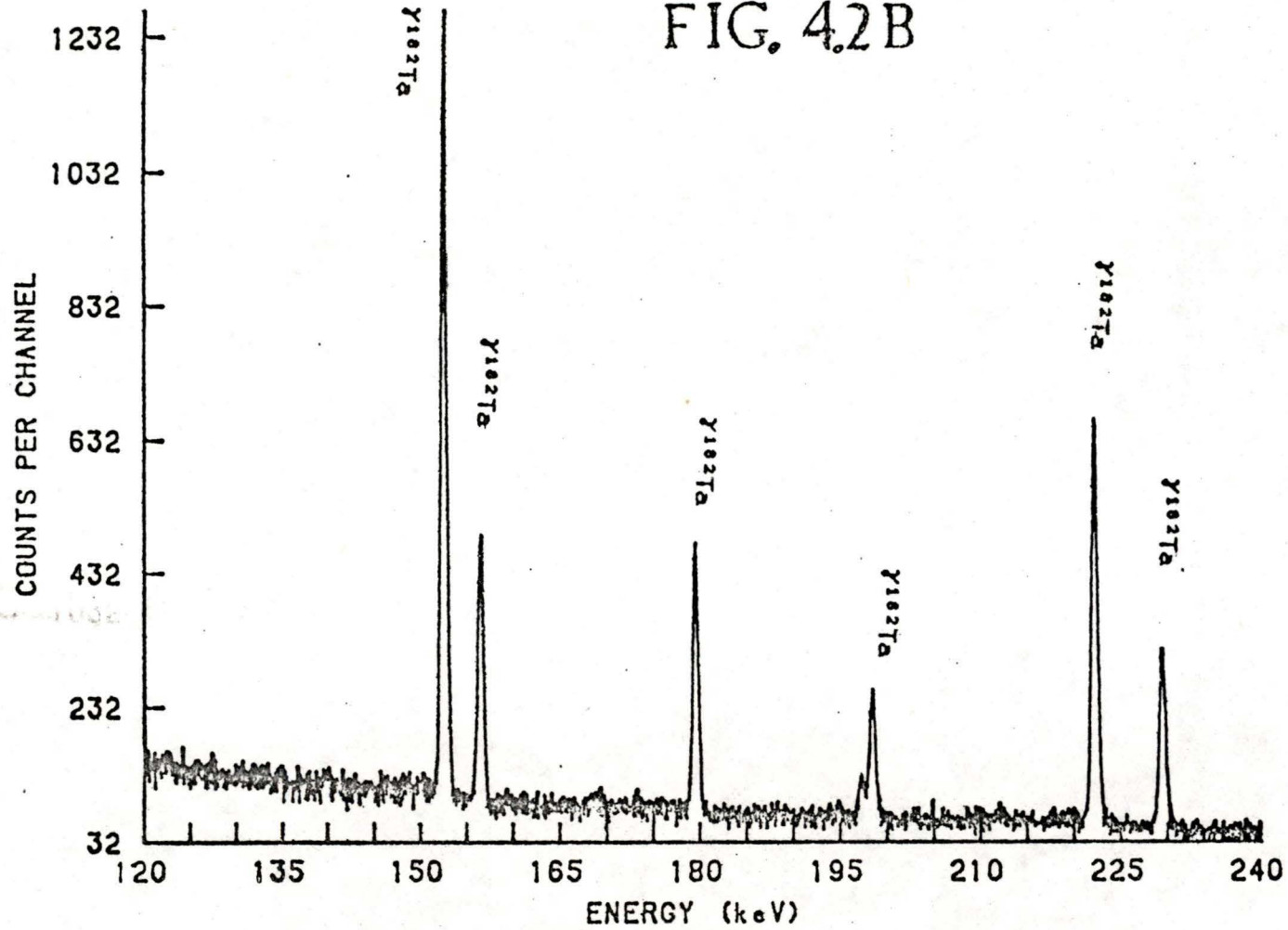
THE ^{13}C CALIBRATION SPECTRUM

FIG. 4.2 A



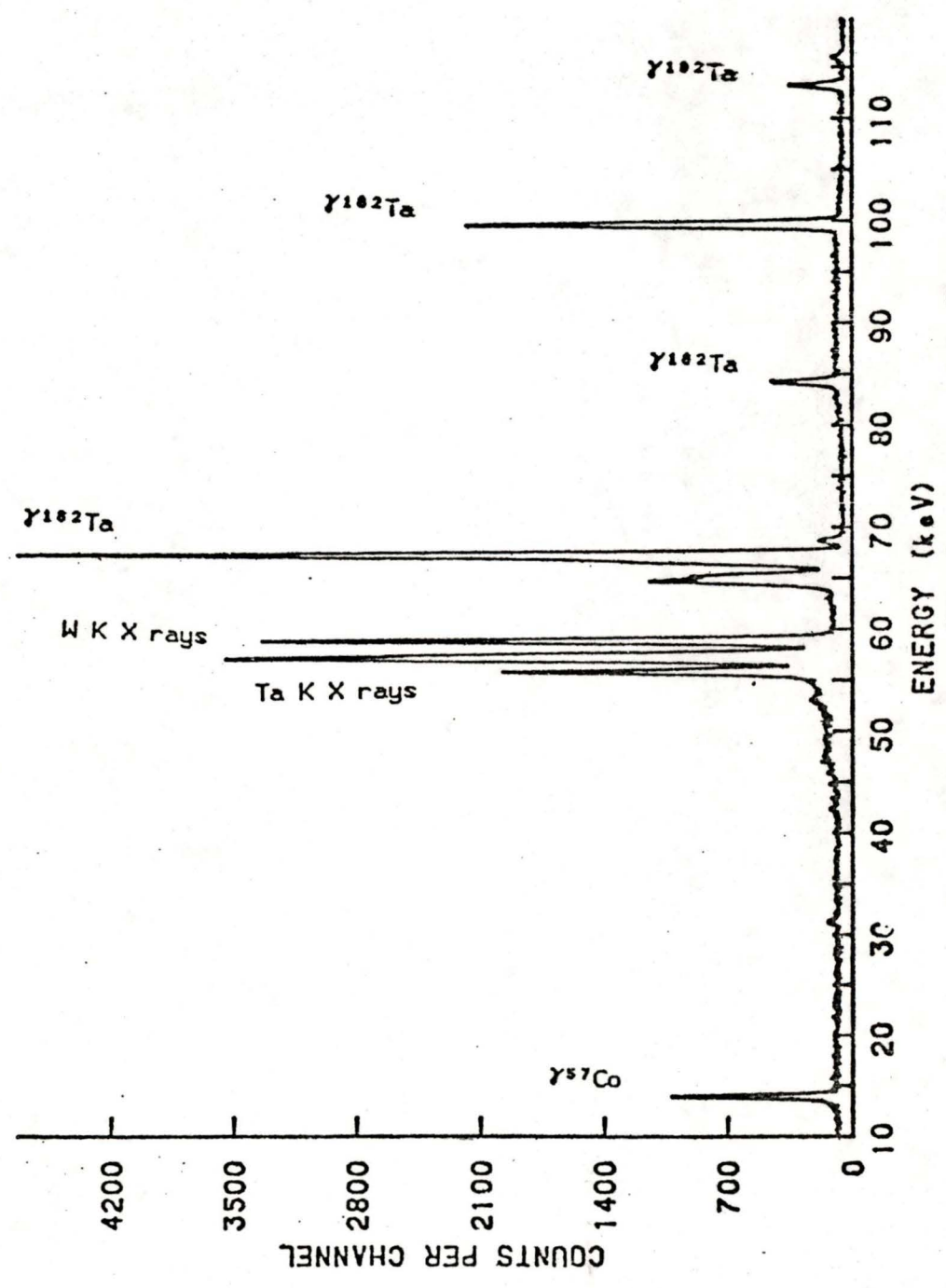
THE ^{12}C CALIBRATION SPECTRUM

FIG. 4.2B



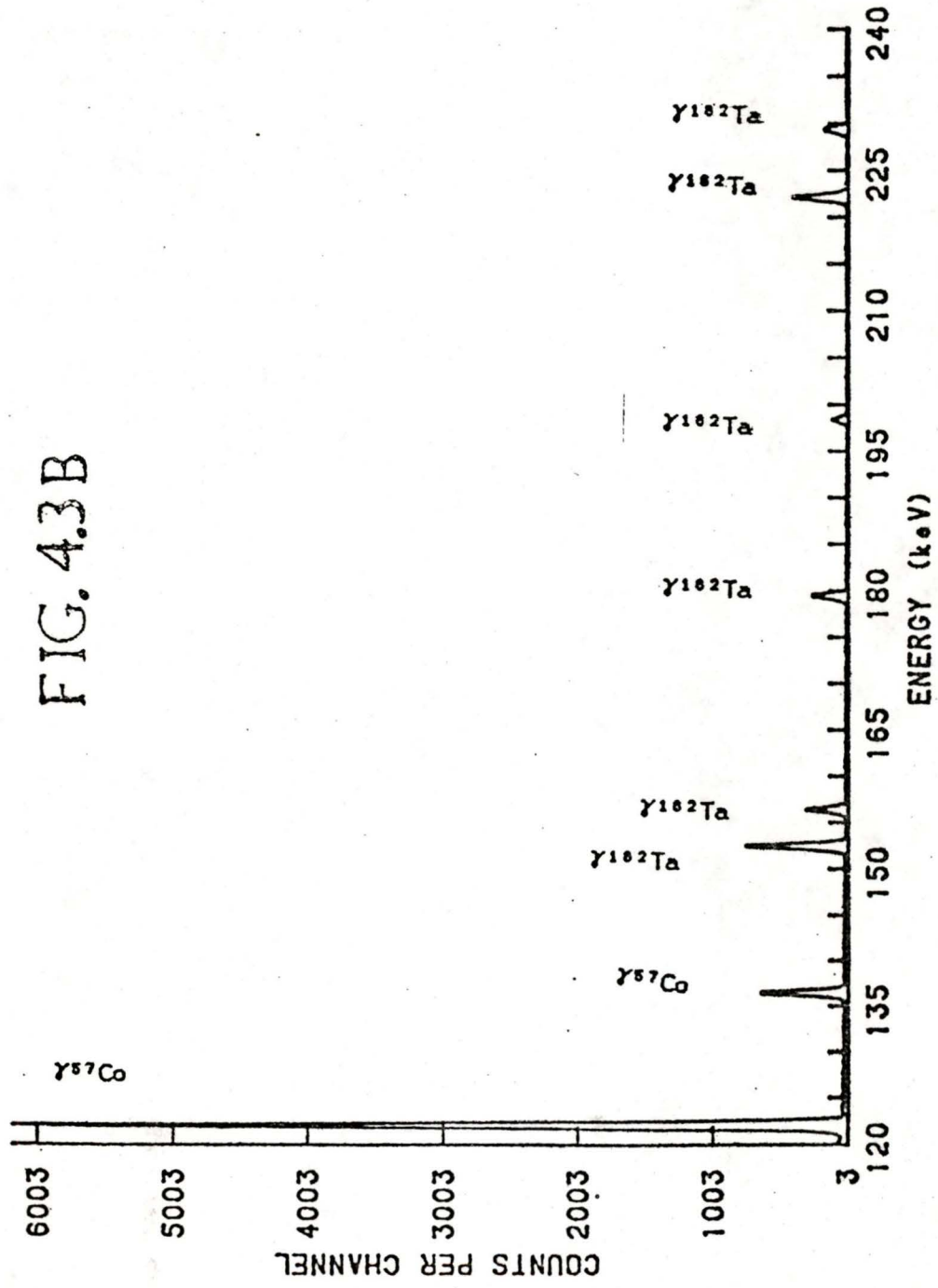
THE ^{12}C CALIBRATION SPECTRUM

FIG. 4.3 A



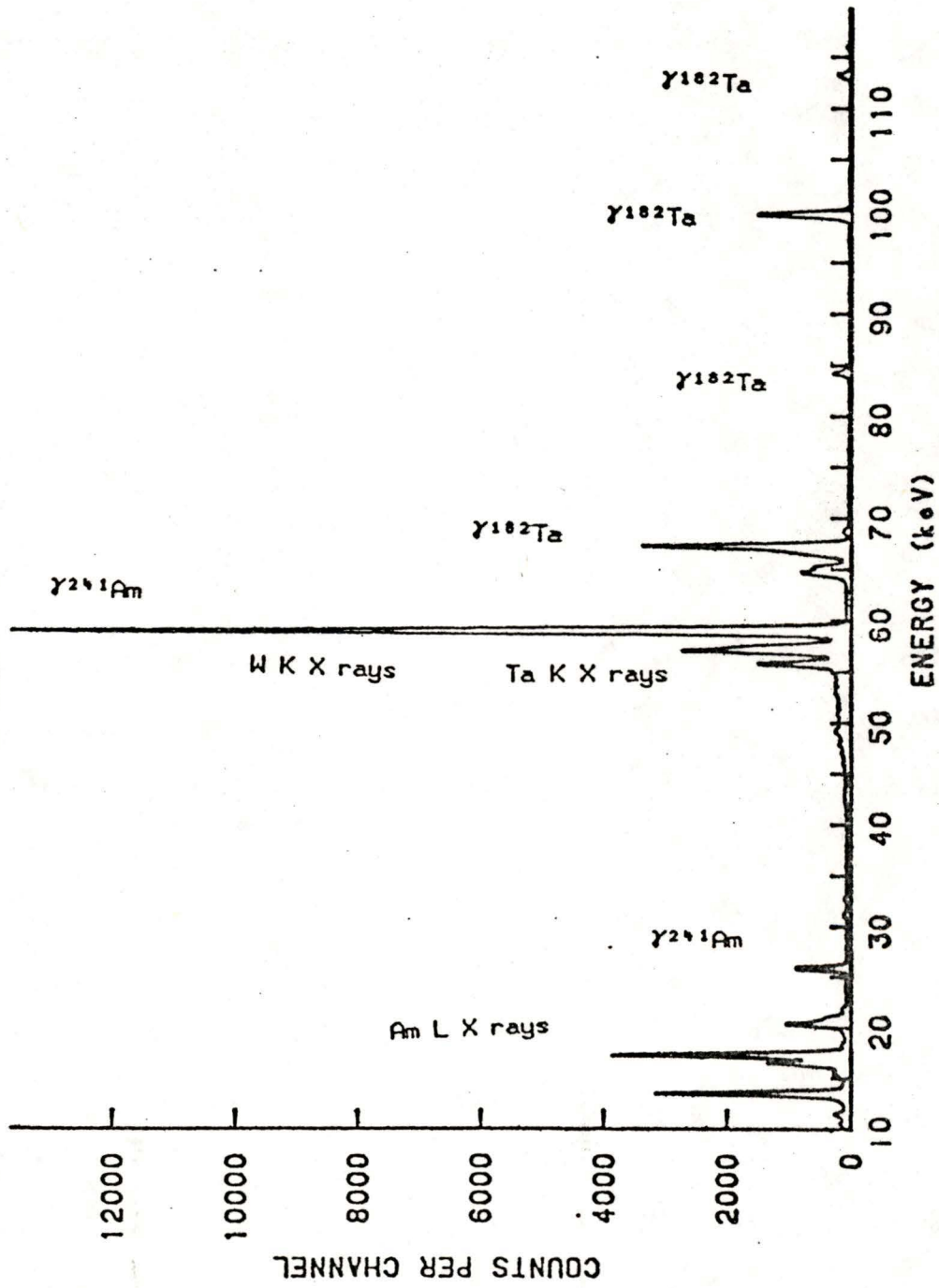
Spectrum of 57 Co and 182 Ta

FIG. 4.3B



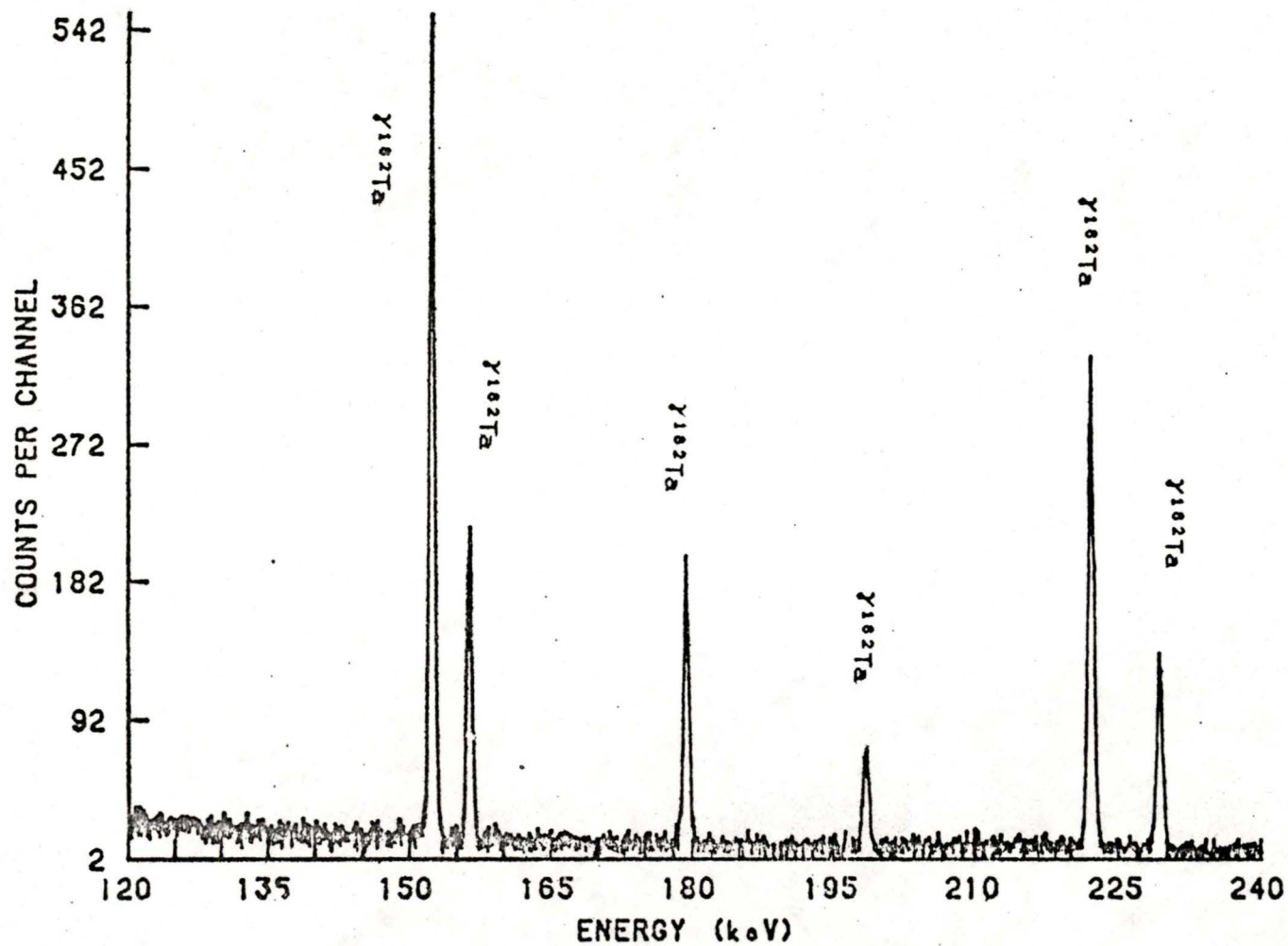
Spectrum of 57 Co and 182 Ta

FIG. 4.4 A



Spectrum of 241 Am and 182 Ta

FIG. 4.4B



Spectrum of ^{241}Am and ^{182}Ta

ponential tails (see Chapter 3). The results of these fits were used to determine efficiency and energy calibration as well as the lineshape parameters FWHM, EXT1, EXT2.

4.1 Energy Calibration

The peak positions obtained from the fits of the calibration spectra above were used to derive linear calibrations of energy as a function of channel number. Two methods of calibration were employed:

- (a) Weighted least squares: l_2 ;
- (b) Weighted least absolute value: l_1 .

Method (b) above was used as a check of method (a) since l_1 approximations are less influenced by the inclusion of erroneous data, that is data containing errors which are not normally distributed as is the case for a calibration peak which contains an unresolved contaminant. For example, the ^{182}Ta 100 keV line turned out to be unsuitable for calibration purposes for this reason as it contained some unresolved contaminants (μCu 7-4 & μAl 5-2). This is also indicated in Section 4.3 where the peak has a larger FWHM than predicted

The results of method (a), using the data in Table III, are listed in Table IV. All uncertainties are standard deviations.

In order to obtain an accurate energy value for the πC

Table III

Peaks used in the energy calibration.

Peak Identity	Standard Energy [1] (keV)	Peak Position (channels)	
		$\pi^{12}\text{C}$ Spectrum	$\pi^{13}\text{C}$ Spectrum
μN 3-2	19.030 \pm .006 [3]	—	144.00 \pm .10
μAl 4-3	23.073 \pm .001 [4]	—	210.74 \pm .20
$\pi^{12}\text{C}$ 4-2	24.815 \pm .008 [2]	239.60 \pm .04	—
πAl 4-3	30.447 \pm .001 [4]	—	332.67 \pm .10
$\gamma^{182}\text{Ta}$	31.735 \pm .001 [5]	353.5 \pm .4	353.92 \pm .12
$\gamma^{182}\text{Ta}$	84.6808 \pm .0003	1229.68 \pm .15	1229.18 \pm .03
$\gamma^{182}\text{Ta}$	152.4308 \pm .0005	2350.0 \pm .2	2349.20 \pm .04
$\gamma^{182}\text{Ta}$	179.3948 \pm .0005	2795.9 \pm .2	2794.91 \pm .05

[1] Standard energies, other than those footnoted are from R. G. Helmer et al., (1978).

[2] T. von Egidy et al., (1974).

[3] Engfer (1974).

[4] Backenstoss et al., (1973).

[5] D. H. White et al., (1970).

3d-2p transition, it was necessary to calibrate the lower energy part of the $\pi^{12}\text{C}$ spectrum to the $\pi^{12}\text{C}$ 4f-2p energy given by von Egidy et al. (1974) and the $\pi^{13}\text{C}$ spectrum to the μN 3d-2p transition energy (Engfer, 1974), μAl 4d-3p and πAl 4d-3p transition energies (Backenstoss, 1973).

Table IV

Linear energy calibration: $E = A + B \cdot \text{channel}$
in keV.

Spectrum

^{12}C : $A = 10.3284 \pm .0064$ keV

$B = .060468 \pm .0000035$ keV/channel

covariance (A,B) = -1.8×10^{-6}

^{13}C : $A = 10.3256 \pm .0013$ keV

$B = .0604914 \pm .0000007$ keV/channel

covariance (A,B) = $-.8 \times 10^{-9}$

4.2 Detector Efficiency

The detector efficiency is defined as the probability that a photon is detected with full photo peak energy by the detection system. The factor due to the solid angles subtended by the detector and source may be neglected if only relative instead of absolute efficiency is required. This is because the solid angles subtended by the source and Germanium detector, vary only slightly with energy. It is therefore possible to determine with a fair degree of accuracy the relative efficiency of the detector without the need to specify accurately the parameters such as source to detector distance and source strength. It is however necessary to know the source thickness and the thickness of any absorbers which may be between the source and detector so correction can be made for the absorption.

If efficiency varies significantly over the region of the fit, it will be necessary to modify the Lorentz-Gauss convolution used in the fit. A knowledge of relative efficiency is also required when calculating the $2p-1s$ transition yield in pionic carbon to determine the strong interaction broadening of the $2p$ level (section 7.1).

4.2.1 The Method of Efficiency Determination

Tantalum (^{182}Ta), Americium (^{241}Am), and Cobalt (^{57}Co) radioactive sources were used as calibration standards to determine the experimental detection efficiency over the range of energies from 14 keV to 230 keV. The standard intensities of

the γ rays and X rays emitted by these sources are listed in Tables V, VI, and VII. The source spectrum peaks were fit to determine their intensities (see Chapter 3). The relative efficiencies thus determined are listed in Tables V, VI, and VII. There was no observable difference in detector efficiency in beam and out of beam.

Since the sources used are of non-zero thickness there is some attenuation of the emitted photons, particularly those at lower energies. The expression for the transmission T of photons emitted by a source of uniform thickness d is:

$$T = \frac{\int_0^d \exp(-\sigma x) dx}{\int_0^d dx}$$

$$= (1 - \exp(-\sigma d)) / \sigma d \quad \dots(4.1)$$

σ is the cross-section for any scattering which degrades the energy of the photon, i.e. σ is the sum of the photo-electric and incoherent scattering cross-sections (pair production does not occur at these energies). The corrections for attenuation in ^{241}Am and ^{57}Co were negligible, however corrections to the ^{182}Ta intensities were appreciable since the source was .005 inches thick. The photon cross-section for tantalum is shown in figure 4.5. The cross-section values used were interpolated

Table VRelative Efficiency from ^{182}Ta (.005 inch foil)

γ -ray Energy (keV)	Relative Standard Yield ⁽¹⁾	Cross Section (cm ² /g)	Relative Efficiency
65.7	.20±.01 ⁽²⁾	2.45	2.07±.17
67.7	2.99±.15	11.23	1.95±.14
84.7	.191±.001	6.25	1.63±.10
100.1	1.00±.03	3.94	1.47±.06
113.7	.133±.004	2.81	1.32±.08
116.4	.031±.001	2.64	1.19±.13
152.4	.502±.002	1.29	.899±.04
156.4	.190±.006	1.21	.875±.04
179.4	.223±.007	.838	.673±.04
198.4	.106±.003	.642	.572±.04
222.1	.537±.017	.476	.457±.02
229.3	.260±.007	.437	.437±.03

⁽¹⁾ All values other than those footnoted are from Gerhke et al., (1977).

⁽²⁾ D. H. White et al., (1970).

Table VIRelative Efficiency from ^{241}Am

Photon Energy (keV)	Absolute Standard Yield ^[1] (photons/decay)	Measured Relative Efficiency ^[2]	
		A	B
13.9 L α X rays	.135 \pm .003	.495 \pm .01	1.07 \pm .04
17.8 L β X rays	.210 \pm .004	.544 \pm .02	1.18 \pm .05
20.8 LY X rays	.050 \pm .001	.557 \pm .02	1.20 \pm .06
26.4 γ ray	.025 \pm .002	.701 \pm .04	1.51 \pm .09
33.2 γ ray	.001 \pm .0001 ^[3]	.885 \pm .15	1.91 \pm .32
59.5 γ ray	.359 \pm .006	1.00 \pm .03	2.16 \pm .11

Table VIIRelative Efficiency from ^{57}Co

Photon Energy (keV)	Absolute Standard Yield ^[1] (photons/decay)	Measured Relative efficiency ^[4]	
		A	B
14.4 γ ray	.095 \pm .002	1.09 \pm .03	1.11 \pm .04
122.0 γ ray	.856 \pm .003	1.20 \pm .01	1.18 \pm .01
136.3 γ ray	.1075 \pm .003	1.00 \pm .01	1.02 \pm .01

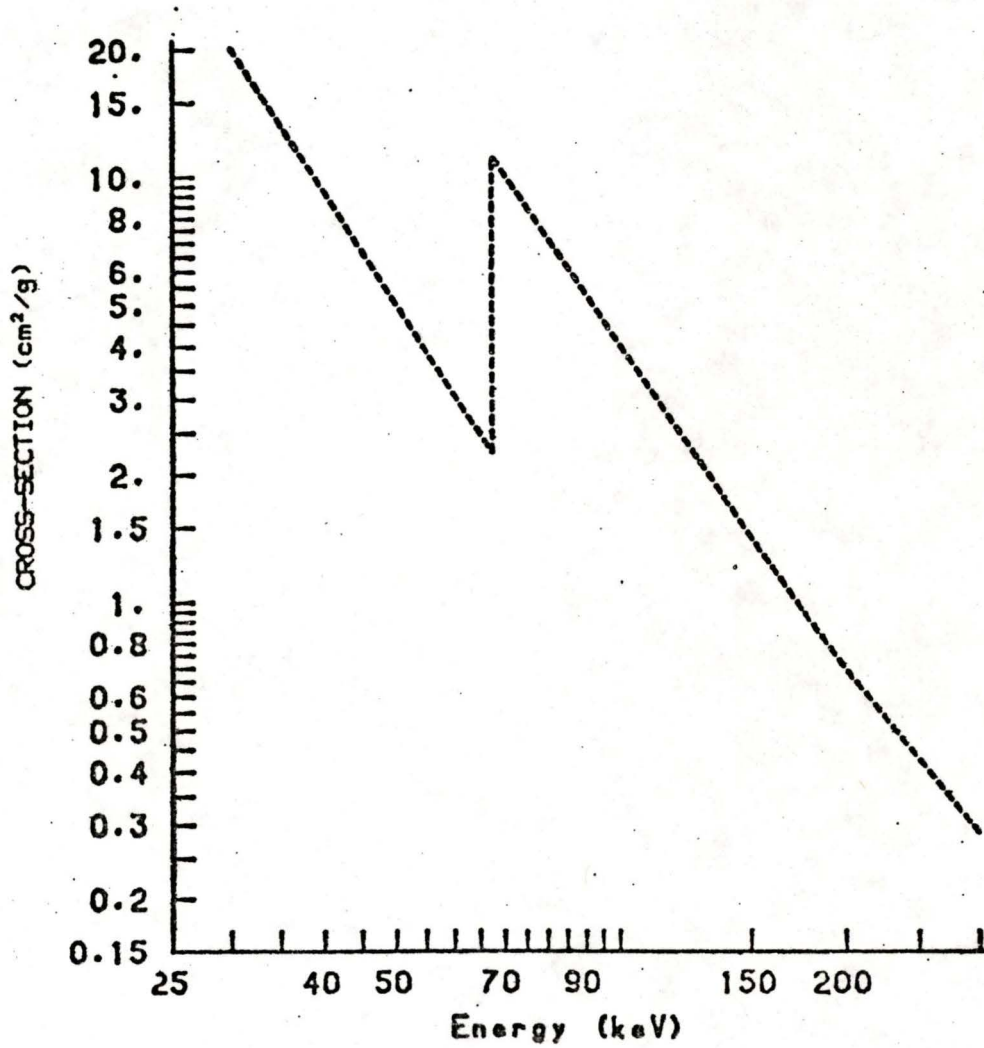
^[1] All values other than those footnoted are from J. S. Hansen et al., (1977).

^[2] Values in column A are normalised to efficiency at 59.5 keV, values in column B to the efficiency curve (see text).

^[3] R. J. Gerhke and R. A. Lokken, (1971).

^[4] Values in column A are normalised to efficiency at 136.3 keV, values in column B to the efficiency curve (see text).

FIG. 4.5



PHOTON CROSS-SECTION FOR TANTALUM

from values listed in Storm and Israel [1] using a power law in energy as the interpolation function [2].

To determine the relative efficiency shown in figure 4.6, a smooth curve was first drawn through or near the efficiency values as determined from fits of the ^{182}Ta source peaks. From this curve values of the relative efficiency for the γ rays at 122 keV and 136 keV of ^{57}Co were interpolated, thus determining the normalisation of the effective ^{57}Co source strength to that of ^{182}Ta . The efficiency at 14.4 keV was then determined from the observed intensity of the 14.4 keV γ ray. This then made possible, the normalisation of the ^{241}Am source to the efficiency curve at 13.9 keV and 59.5 keV thus determining the relative efficiency over the range 14 to 230 keV.

To incorporate the relative efficiency into the fitting procedure it was approximated by an exact fit of a rational function, shown in figure 4.6. The rational function $Q(x)$ is a quotient of polynomials:

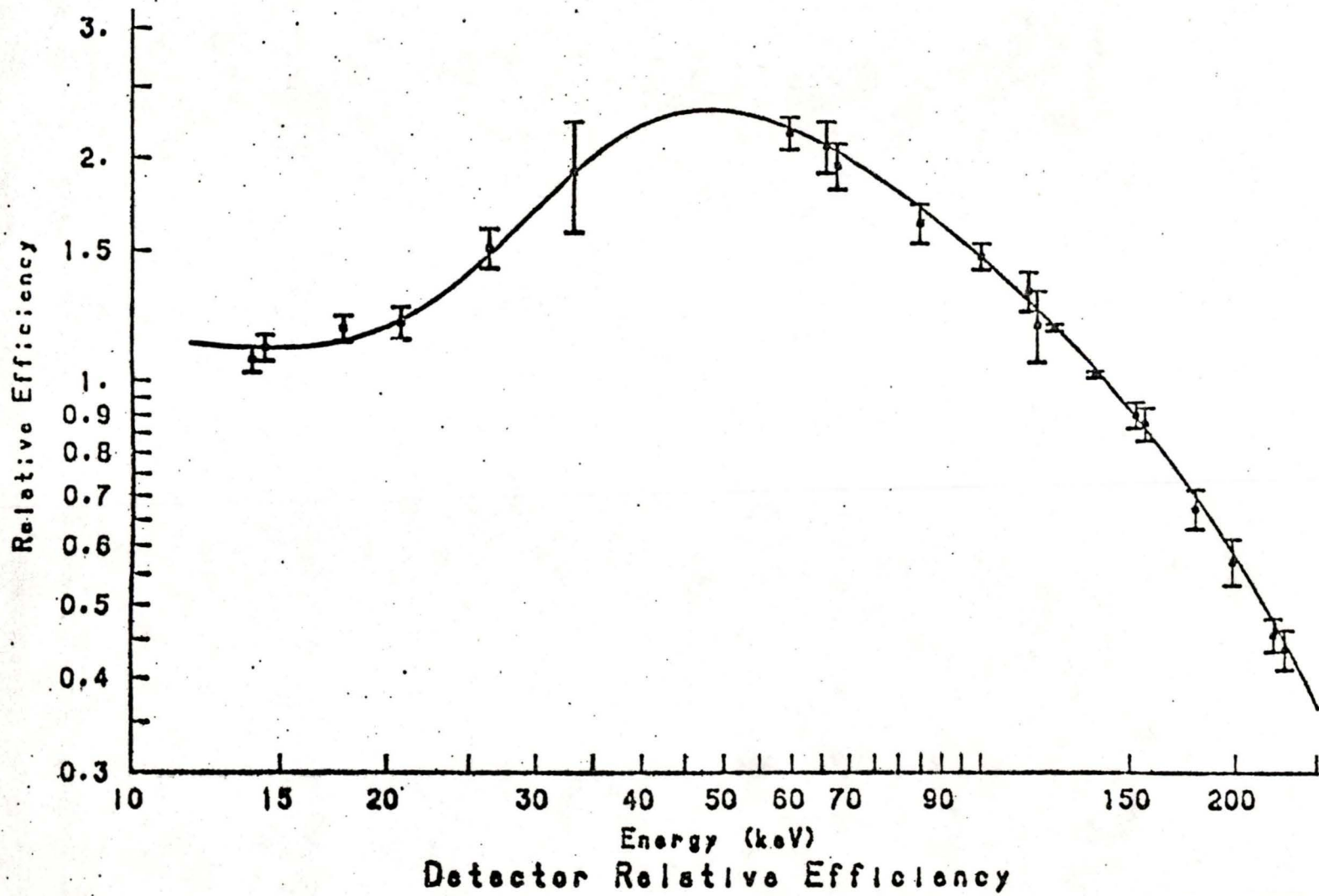
$$Q(x) = \frac{-1+a_1x+a_2x^2+a_3x^3+a_4x^4}{b_1+b_2x+b_3x^2+b_4x^3} \quad \dots(4.2)$$

where a_i and b_i are constants to be determined (see Table VII)

[1] Storm and Israel, (1970).

[2] The shape of figure 4.5 suggests that σ depends upon the product of some power of the energy E and a constant, to a good approximation over a range of energies not spanning any absorption edges, i.e. for continuous σ .

FIG.4.6



and x is the energy in keV.

Table VII

Constants in the rational function $Q(x)$

a_1	$.619 \times 10^{-1}$
a_2	$-.174 \times 10^{-2}$
a_3	$.632 \times 10^{-5}$
a_4	$-.669 \times 10^{-8}$
b_1	$-.699$
b_2	$.262 \times 10^{-1}$
b_3	$-.370 \times 10^{-3}$
b_4	$-.275 \times 10^{-5}$

4.3 Lineshape

4.3.1 FWHM

It is well known that the detector resolution or FWHM of purely Gaussian peaks varies with energy in the following way: [1]

$$(\text{Total FWHM})^2 = (\text{FWHM due to noise})^2 + F (2.35)^2 \epsilon E \dots (4.3)$$

where the FWHM due to noise is a constant depending on the electronics, $F \approx .13$ is the Fano factor, $\epsilon \approx 2.98$ eV is the electron hole pair production energy and E is the energy in eV.

[1] Kevex Corporation

For our purposes it is sufficient to note that the square of the total FWHM is a linear function of energy E. The data in Table IX were fit to the expression:

$$(\text{total FWHM})^2 = A + B \cdot E \quad \dots(4.4)$$

where A and B are constants to be determined, in order to predict the FWHM to be used in the π C 2p-1s fits (chapter 6).

Table IX Variation of FWHM with Energy

Energy (keV)	$\pi^{12}\text{C}$ FWHM (keV)	$\pi^{13}\text{C}$ FWHM (keV)	Results:
85	.54	.54	$\pi^{12}\text{C}$ A = .12 \pm .02 (keV) ² B = .0020 \pm .0001 (keV)
152	.65	.65	
179	.68	.70	$\pi^{13}\text{C}$ A = .11 \pm .02 (keV) ² B = .0020 \pm .0001 (keV)
225	.57	.59	

The values obtained for B agree quite well with the theoretical value of .0021 (keV) predicted by equation (4.3). Using these results it was possible to detect peaks which were contaminated by their telltale FWHM which was larger than predicted.

4.3.2 The Exponential Tailing Parameters EXT1 and EXT2

The exponential tailing parameters could not be determined accurately from fits of source peaks, particularly in the ^{12}C spectrum. The tailing parameters can affect the position and width of a broadened peak very strongly. For this reason the values of EXT1 and EXT2 were kept as free parameters in the fits of the pionic 2p-1s ^{12}C and ^{13}C fits. The values thus determined

are listed in Table X below.

Table X

Exponential tailing parameters determined by fits
of the $\tau^{12}\text{C}$ and $\tau^{13}\text{C}$ 2p-1s regions.

	$\tau^{12}\text{C}$	$\tau^{13}\text{C}$
EXT1	.009±.007	.006±.004
EXT2	.628±.314 keV ⁻¹	1.55±.727 keV ⁻¹

Chapter 5

The Determination of the ^{12}C

Contamination in the ^{13}C Spectra

The isotopic composition of what we will call the " ^{13}C target" is 99.7% ^{13}C and .3% ^{12}C . However, there exists the possibility that the ^{13}C spectrum contains more than .3% ^{12}C contamination because natural carbon is present in the concrete floor, shielding, scintillators, and scintillator wrapping. The amount of ^{12}C contamination assumed in the fitting process affects the positions and widths of the transitions since the Lorentz broadened peaks $\pi^{12}\text{C}$ and $\pi^{13}\text{C}$ 2p-1s are separated by approximately half their Lorentzian half widths. For instance, a .6% ^{12}C contaminant decreases the $\pi^{13}\text{C}$ energy by 4 eV and width by 5 eV. This section attempts to infer the $\pi^{12}\text{C}$ contamination from the intensities of carbon, nitrogen, and aluminum X rays observed in the target-empty run that was acquired using an empty aluminum duplicate of the casing which held the ^{13}C (see Table XI). Since multiple scattering effects in the ^{13}C run are large because of the distance of S_3 and in the target-empty run were much reduced, the observed intensities were normalised to the intensity of the πAl 3d-2p X rays which originated almost entirely from the aluminum casing, rather than to the number of π -stops recorded (see Section 2.3). In view of the fact that the stopping distributions for pions and muons are quite different it is necessary to discuss each

individually.

5.1 Muons

Muon counts in the $\pi^{13}\text{C}$ spectrum arise in three ways:

(i) The distribution of arrival times for pions from the production target and muons from π decay close to the production target overlap somewhat since the momentum interval $\delta p/p$ is 10% and consequently the 8.4 meter flight path is insufficient to separate the two distributions completely at the operating momentum of 88 meV/c. They are fairly well focussed and give rise to counts in the ^{13}C target as well as in the air and other nearby objects.

(ii) Scattered muons which leak through the channel and are ill focussed, stop in the experimental area in random coincidence with the π -stop signal or may even simulate a π -stop signal.

(iii) Pions which decay in flight near the target form a diffuse source of muons which stop in the experimental area in coincidence with a π -stop signal.

The μC $2p$ -1s intensity ratio of the target-empty run to the ^{13}C run was $(6.8 \pm 2)\%$. This value, however, may be an under estimate of the $\mu^{12}\text{C}$ component in the ^{13}C run for two reasons:

(a) The multiple scattering of muons of types (i), (ii), and (iii) is enhanced by the presence of the ^{13}C target, although the range is only negligibly decreased. This effect decreases the effectiveness of veto counter S_3 and allows a sig-

nificant increase in the number of μN counts from air in the ^{13}C run over that observed in the target-empty run.

(b) The diffuse source of muons in (iii) above is more intense in the ^{13}C run than in the target-empty run. This effect also contributes to a rise in the number of μN X rays observed from air.

The ratios of the intensities of μN X rays in the ^{13}C to the target-empty run is 1.88 ± 0.07 (average of the 2-1 and 3-1 X-ray intensities). It is assumed that, since μC counts originate from non-target sources as do the μN X rays, the proportion of $\mu^{12}\text{C}$ X rays to all the μC X rays in the ^{13}C run is limited to a maximum of $(1.88 * 6.8\%) = 13\%$. Recalling that 6.8% was an under estimate, we have finally assigned $(10 \pm 3)\%$ as the $\mu^{12}\text{C}$ component of the μC X rays in the ^{13}C run.

5.2 Pions

The most accurate limit of the $\pi^{12}\text{C}$ contamination of the $\pi^{13}\text{C}$ spectrum was given by the πC 3d-2p X ray: the target-empty signal was found to be less than .08% that in the ^{13}C spectrum. A straight forward use of the 2p-1s transition was not possible because of its large width: viz. the πC 2p-1s target-empty peak indicates a contamination as much as 10% of the $\pi^{13}\text{C}$ 2p-1s peak. The πC 3d-2p peak is a more accurate indicator.

Photons from the πC 3d-2p transition (target-empty run)

could be absorbed, either by the shielding around the detector, or because they originate deep in the concrete floor, shielding or lucite light pipe. The transmission for the π^+C 2p-1s energy of 92 keV would have to be more than fourteen times the transmission for the π^+C 3d-2p energy of 19 keV in order to admit a π^+C 2p-1s contamination of one percent in the target-empty spectrum. This eliminates the possibility of contaminant photons which originate deep in materials such as concrete or lucite because the stopping distribution for the pions in these materials does not permit stops at great enough depths in significant numbers: the momentum and range of the beam of pions were adjusted for maximum stopping rate in $.593 \text{ g/cm}^2$ of carbon whereas $.593 \text{ g/cm}^2$ of lucite or concrete would cause at most a factor of two difference in the transmissions.

The one-half inch copper shielding which surrounded the detector is too thick to be responsible for allowing photons of the π^+C 2p-1s energy through, let alone the π^+C 3d-2p energy. The transmission at 92 keV is less than $.006$ which is too small to allow a significant number of π^+C 2p-1s photons to be detected via this route.

The π^+C 3d-2p intensity in the target empty-run is therefore assumed to indicate accurately the amount of π^+C X rays in the target-empty run. The ratio of the intensity of π^+C 3d-2p X rays in the target-empty run to that in the ^{13}C run is $(.04 \pm .04)\%$. As was the case with muons in section 5.1 above, it is

necessary to correct this ratio for increased multiple scattering and for decreased range of the pions in the ^{13}C run relative to the target-empty run. This is estimated from πN counts in air. The πN 3d-2p intensity in the ^{13}C run is 8.1 ± 2.7 times that in the target-empty run. The πC 3d-2p contamination in the ^{13}C run is increased by this factor, to a value of $(.3 \pm .4)\%$. Finally the isotopic impurity .3% of the ^{13}C target is added to form the estimate of the total πC contamination in the ^{13}C run as $(.6 \pm .4)\%$.

Table XI

Relative Intensities of Various Peaks in the
Target-empty and ^{13}C Spectra.
(normalised to πAl 3d-2p)

<u>Peak</u>	<u>Target-empty</u>	<u>^{13}C</u>
μN 3-2	$.25 \pm .08$	$2.03 \pm .07$
μN 2-1	$.64 \pm .02$	$1.12 \pm .02$
μC 2-1	$.06 \pm .01$	$.82 \pm .06$
πC 3d-2p	$.006 \pm .006$	$16.6 \pm .2$
πC 2p-1s	$.0 \pm .4$	$.20 \pm .01$
πAl 3d-2p	<u>$1.00 \pm .02$</u>	<u>$1.00 \pm .01$</u>

Chapter 6

The Determination of the π C 2p-1s

Energies, Widths and Strong Interaction Shifts

The data obtained for the π C 2p-1s transitions (Fig. 2.6 b and 2.7 b) were fit using the procedure described in Chapter 3. Where possible, parameters of the fit were fixed at values determined by other methods: the lineshape parameter FWHM was fixed at a value obtained through interpolation of the values from fits of clean source peaks in the calibration spectra (see Chapter 4). Certain peaks which have well known energies were fixed at those energies using the energy calibration obtained from the source spectra as well. The lineshape parameters EXT1 and EXT2 were determined statistically during the fitting process.

The results of the fitting procedure are as follow:

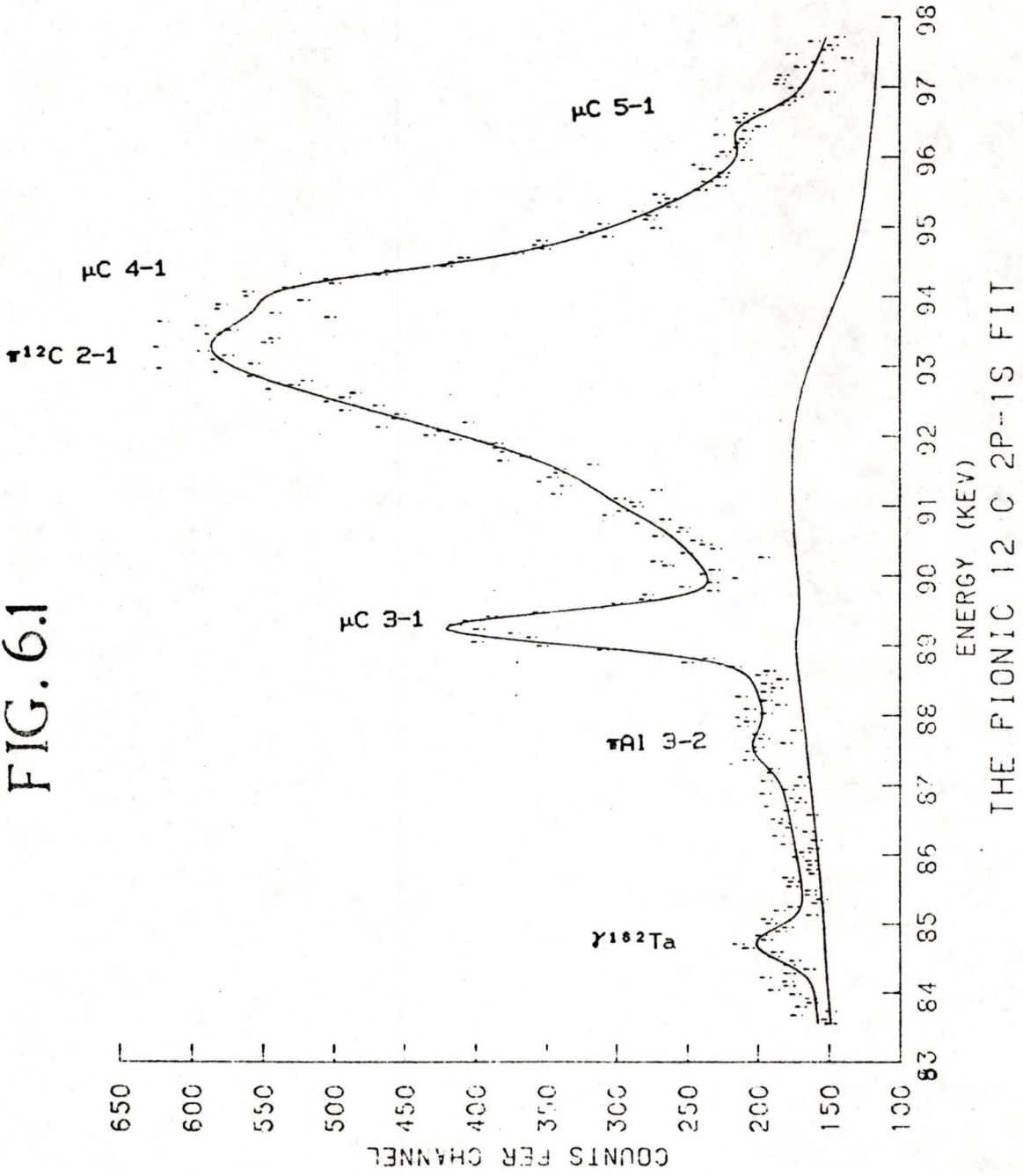
Transition	Energy (keV)	Width (keV)
$\pi^{12}\text{C}$ 2p-1s	93.287 \pm .043	2.65 \pm .120
$\pi^{13}\text{C}$ 2p-1s	92.227 \pm .027	2.59 \pm .110

Discussion of each of ^{12}C and ^{13}C fits, shown in figures 6.1 and 6.2 follows.

6.1 The $\pi^{12}\text{C}$ Fit

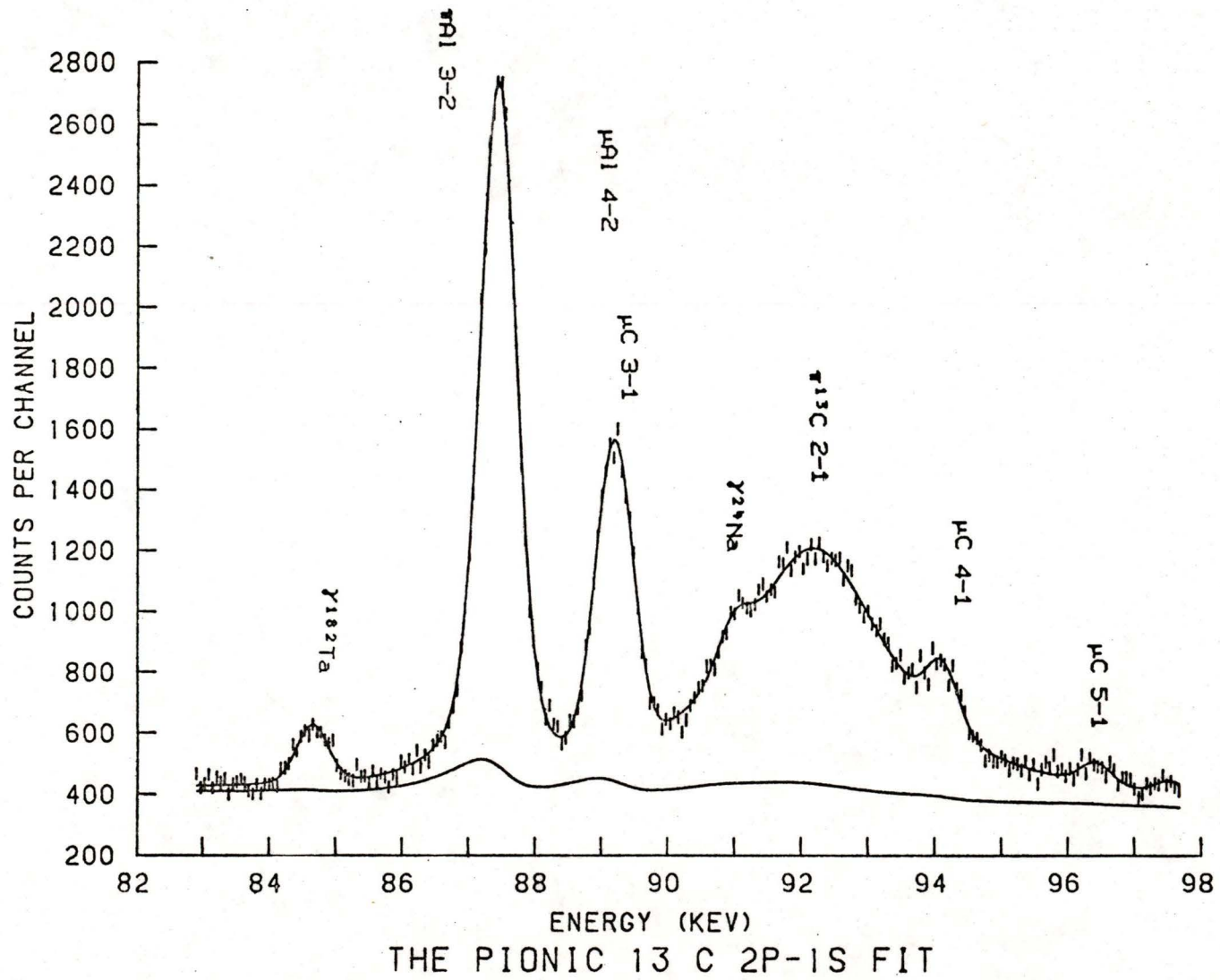
In the least squares fit of the $\pi^{12}\text{C}$ 2p-1s transition it was necessary to include a 1.11% ^{13}C component which is the natural abundance of ^{13}C in natural graphite. Neglecting this ^{13}C component would have decreased the $\pi^{12}\text{C}$ 2p-1s energy by about 12 eV

FIG. 6.1



THE PIONIC 12 C 2P--1S FIT

FIG. 6.2



and increased the width by 20 eV. The statistical uncertainties of the energy and width for the $\pi^{12}\text{C}$ 2p-1s peak were calculated with the parameters listed in Table XII, fixed. Additional uncertainties ΔE and $\Delta \Gamma$ in the energy and width are also listed in Table XII computed by variation of each fixed parameter within limits specified by the accuracy to which its value was known. Finally uncertainties in the energy calibration and due to the choice of a finite fitting region or window were computed. These uncertainties were then totalled in quadrature to form estimates of the total uncertainties of the width Γ and energy E .

6.2 The $\pi^{13}\text{C}$ Fit

The broadened $\pi^{13}\text{C}$ 2p-1s peak was fitted using the method described in Section 6.1 above. The fixed parameters of the fit are listed in Table XIII. Due to the relative smallness of the ^{13}C target, contaminant lines in this fit are large compared to those in the $\pi^{12}\text{C}$ fit, hence contributing more to the total uncertainty. On the other hand uncertainty due to the proximity of the μC 4f-3d transition is reduced in the ^{13}C case relative to the ^{12}C case. The $\pi^{12}\text{C}$ contamination (Chapter 5) also contributes significantly to the total uncertainty. The lineshape parameters however are much more well determined in this case than the ^{12}C case since the statistics accumulated in the source spectrum are much greater. Another source of uncertainty is the possible existence of peaks whose intensities are so low as to be not conclusively labelled as

TABLE XII

Various contributions to the uncertainty in the $\pi^{13}\text{C}$ 2p-1s energy E and width Γ .

<u>Fixed Energy</u>	ΔE (eV)	$\Delta \Gamma$ (eV)
πAl 3d-2p	0	0
μAl 4f-3d	1	0
$\pi^{13}\text{C}$ 2p-1s	0	0
μC 3d-2p	1	0
μC 4f-3d	1	12
$\gamma^{23}\text{Na}$	1	12
<u>Fixed Widths</u>		
πAl 3d-2p	0	0
$\pi^{13}\text{C}$ 2p-1s	1	12
<u>Fixed Lineshape</u>		
FWHM	1	6
<u>Statistical</u>	43	110
<u>Window</u>	7	12
<u>Energy Calibration</u>	2	0
<u>Total</u>	43	115

Table XIII

Various contributions to the uncertainty in the $\tau^{13}\text{C}$ 2p-1s energies and widths

<u>Fixed Energies</u>	ΔE (eV)	$\Delta \Gamma$ (eV)
μC 3-1	2	24
μC 4-1	1	0
$\gamma^{23}\text{Na}$	0	24
μAl 4-2	5	18
$\tau^{12}\text{C}$ 2p-1s	1	6
<u>Fixed Widths</u>		
$\tau^{12}\text{C}$ 2p-1s	2	6
<u>Fixed Lineshape</u>		
FWHM	4	6
<u>Statistical</u>	17	64
<u>Unknowns</u>	13	30
<u>Window</u>	5	61
<u>$\tau^{12}\text{C}$ contamination</u>	4	6
<u>Calibration</u>	2	0
<u>Total</u>	27	110

peaks in the fit. As in Section 6.1 above the uncertainties listed in Table XIII are combined in quadrature to estimate the total uncertainty in E and Γ .

6.3 Strong Interaction Shifts of the 1s level in π C

It is possible to extract from the observed 2p-1s transition energies, the strong interaction shift of the 2p-1s energies in $\pi^{12}\text{C}$ and ^{13}C . The 1s shift is large and is largely responsible for the shift in the 2p-1s transition energy since the shift of the 2p level is only about 1 eV. The binding energy of the 1s level is reduced by the strong interaction while the binding energy of the 2p level is slightly increased in the case of carbon. This means the 2p-1s transition energy is reduced. The strong interaction shift of the 2p-1s transition is defined as the difference between the observed energy and the energy calculated, including all effects except those due to the strong interaction.

The energies in Table XIV were calculated using the program PIATOM (Krell, 1977). The calculation includes vacuum polarization and finite extent of the nucleus, solving a Klein-Gordon type of equation numerically for the complex eigenvalues which determine the energies and widths of the various levels in pionic carbon. The calculation also makes use of the r.m.s. charge radii determined for ^{12}C and ^{13}C from muonic X ray energy measurements (Appendix B).

Table XIVStrong Interaction Shifts

Level or Transition	Calculated Energy No strong interaction (keV)	Strong Interaction Shift (keV)
$\tau^{12}\text{C}$ 2p-1s	99.061	-5.774 \pm .043
2p	-33.087	
1s	-132.148	
$\tau^{13}\text{C}$ 2p-1s	99.154	-6.927 \pm .027
2p	-33.118	
1s	-132.272	

Chapter 7

The Determination of the 3d-2p Transition

Energy and Width in $\pi^{12}\text{C}$ and $\pi^{13}\text{C}$

7.1 The 3d-2p Transition Energy in πC

The 3d-2p peak was fit using the method described in Chapters 3 and 6. It was necessary to include a small $\pi^{12}\text{C}$ contaminant in the $\pi^{13}\text{C}$ fit (see Fig. 7.1). The energy for the $\pi^{12}\text{C}$ 3d-2p transition thus obtained was $18.400 \pm .006$ keV and for ^{13}C , $18.427 \pm .002$ keV. The uncertainties are dominated by uncertainties in the energy calibration at this energy. Lineshape parameters were determined by the statistics of the fit and hence uncertainties in these are included in the statistical uncertainty which was .001 keV.

7.2 The Width of the 2p level in $\pi^{12}\text{C}$ and ^{13}C

The width Γ of the 2p level in pionic C can be determined by using the method of relative intensities, described by H. Koch (1975). We define:

$$\begin{aligned} \alpha &= \Gamma_r / (\Gamma_r + \Gamma_s + \Gamma_a) \\ &\simeq \Gamma_r / (\Gamma_r + \Gamma_s) \end{aligned} \quad \dots (7.1)$$

where Γ_r , Γ_s , and Γ_a are the radiative, strong interaction, and Auger widths for the 2p level respectively. Clearly, α is the ratio of the 2p-1s X-ray rate to the total transition rate from the 2p level. The latter is also the sum of the 3d-2p, 4f-2p, 5g-2p, etc. X rays, so that α can be obtained

from the X-ray intensities after appropriate corrections for the change in detector efficiency with energy. Γ is calculated using the program PIATOM (Krell, 1977), taking into account all electromagnetic and strong interaction effects and integrating the wavefunction numerically to find the transition rate, and hence the width.

The measured intensities of the transitions to the 2p level are listed in Table XV. These values are corrected not only for variation in relative detection efficiency, but also for absorption within the $\pi^{13}\text{C}$ target and by its aluminum casing and for absorption in the graphite slab in the case of ^{12}C , using a program due to Mausner (1977) (see Fig. 7.5 & 7.6). The fits are shown in figures 7.1, 7.2, 7.3, and 7.4. The error due to neglecting transitions higher than 6h-2p is negligible.

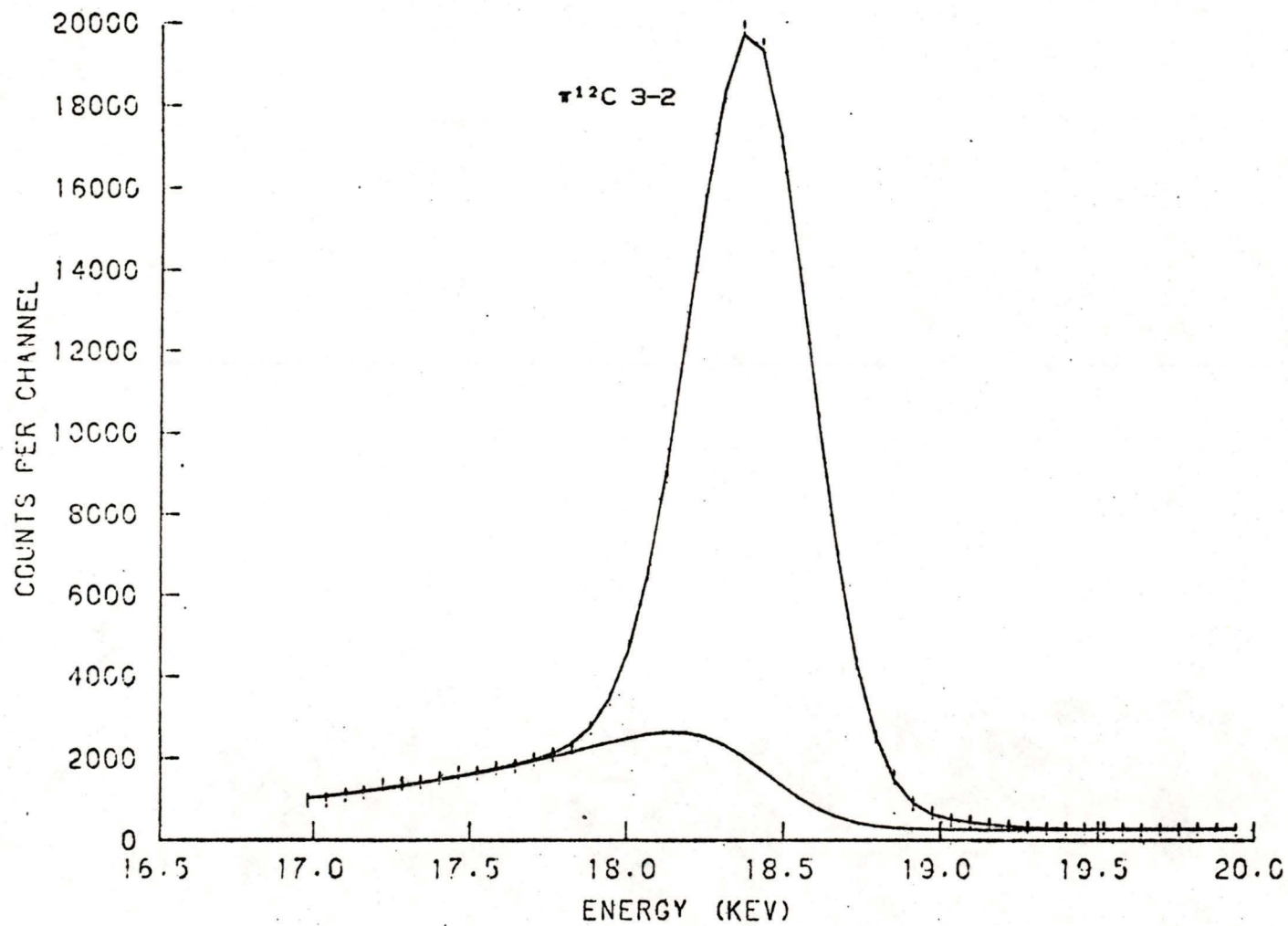
Table XV

Intensities of various transitions used in the determination of the 2p level width Γ_s .

Transition	Relative Intensity		
	^{12}C (1)	^{13}C (2)	^{12}C (3)
2p-1s	.127 \pm .004	.151 \pm .004	—
3d-2p	1.000 \pm .007	1.00 \pm .05	1.00 \pm .14
4f-2p	.168 \pm .002	.197 \pm .007	.18 \pm .02
5g-2p	.027 \pm .005	.026 \pm .001	.02 \pm .01
6h-2p	.0057 \pm .0003	.0060 \pm .0004	—

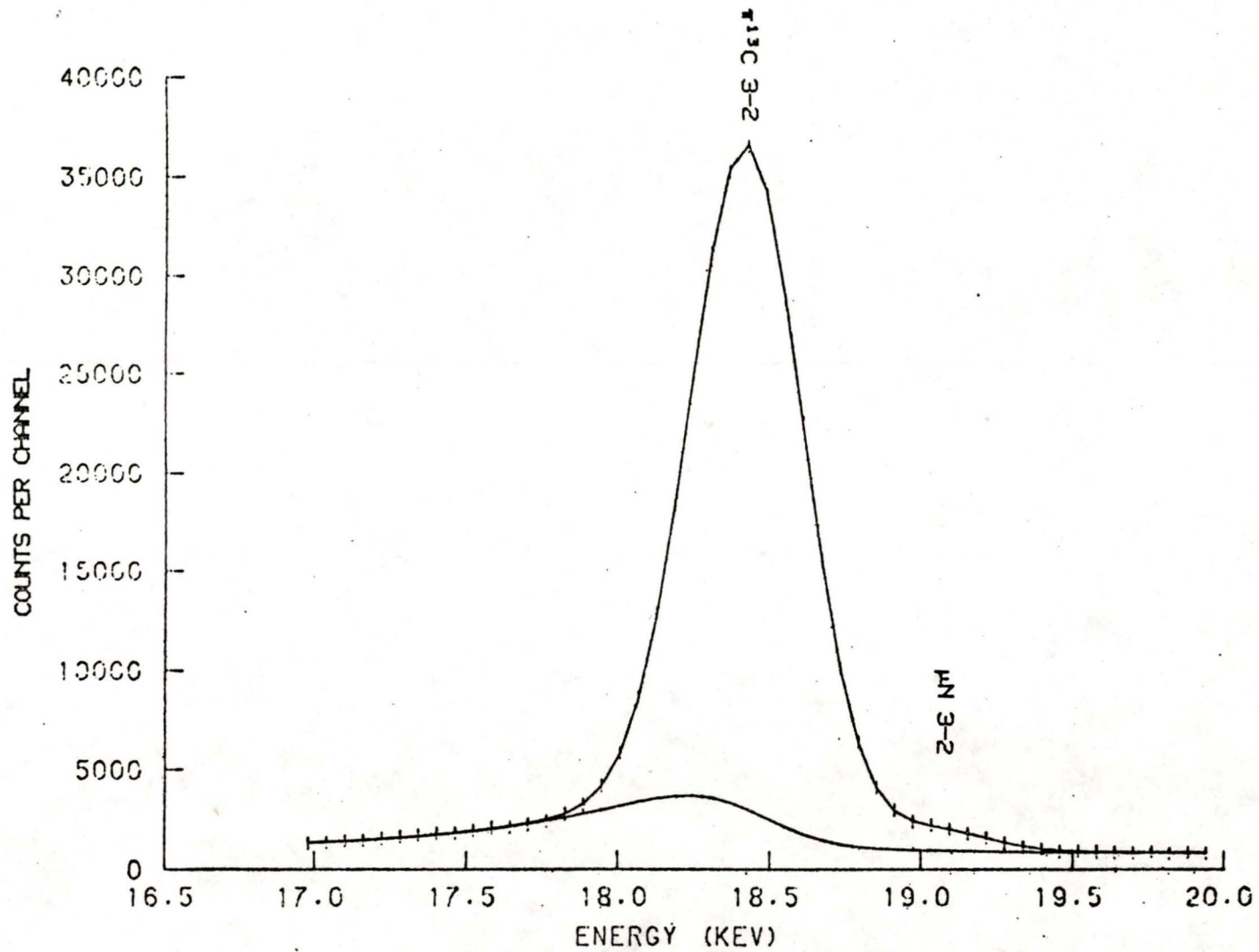
	^{12}C (1)	^{13}C (2)
Total Population of the 2p level	1.20 \pm .02	1.23 \pm .06
α	.106 \pm .009	.151 \pm .004
Γ_r	.138 eV	.137 eV
Γ_s	1.17 \pm .11 eV ⁽⁴⁾	.97 \pm .10 eV

- (1) Values for graphite, corrected for absorption in 1.42 g/cm² slab of graphite at 45°.
- (2) Intensity values are corrected for absorption in .593g/cm² of carbon and for absorption by .0069 g/cm² of aluminum. The correction for carbon was done using a program due Mausner (1977) and absorption cross sections from Storm and Israel (1970) shown in figures 7.1 and 7.2.
- (3) Values for graphite tabulated by T. von Egidy (1974).
- (4) Previous result for ^{12}C is $\Gamma_s = 1.02\pm.29$ eV (H. Koch, 1969).



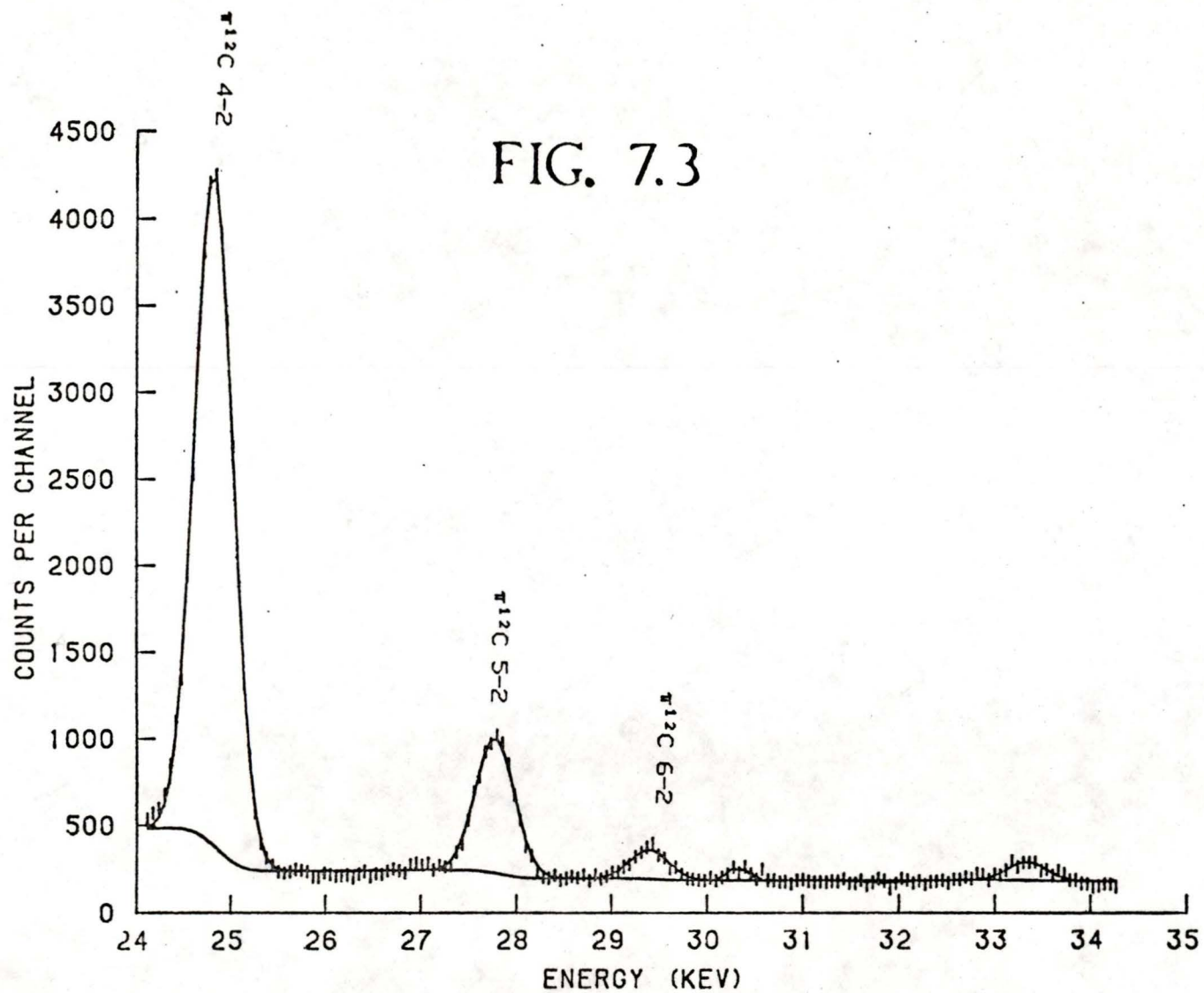
THE PIONIC ^{12}C 3D-2P FIT

FIG. 7.1



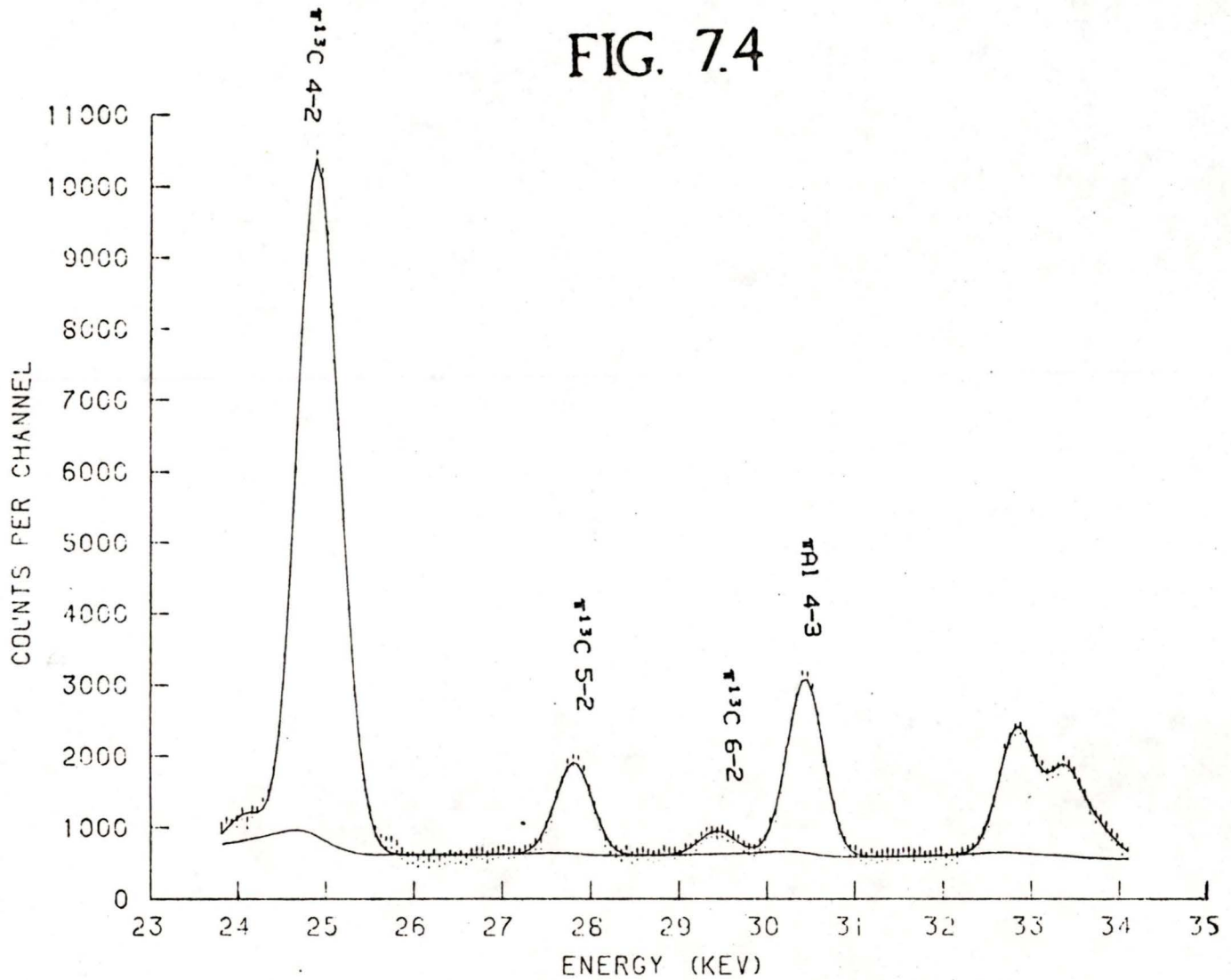
THE PIONIC 13 C 3D-2P FIT

FIG. 7.2



FIT OF THE PIONIC 12 C L-SERIES

FIG. 7.4



FIT OF THE PIONIC ^{13}C L-SERIES

FIG. 7.5

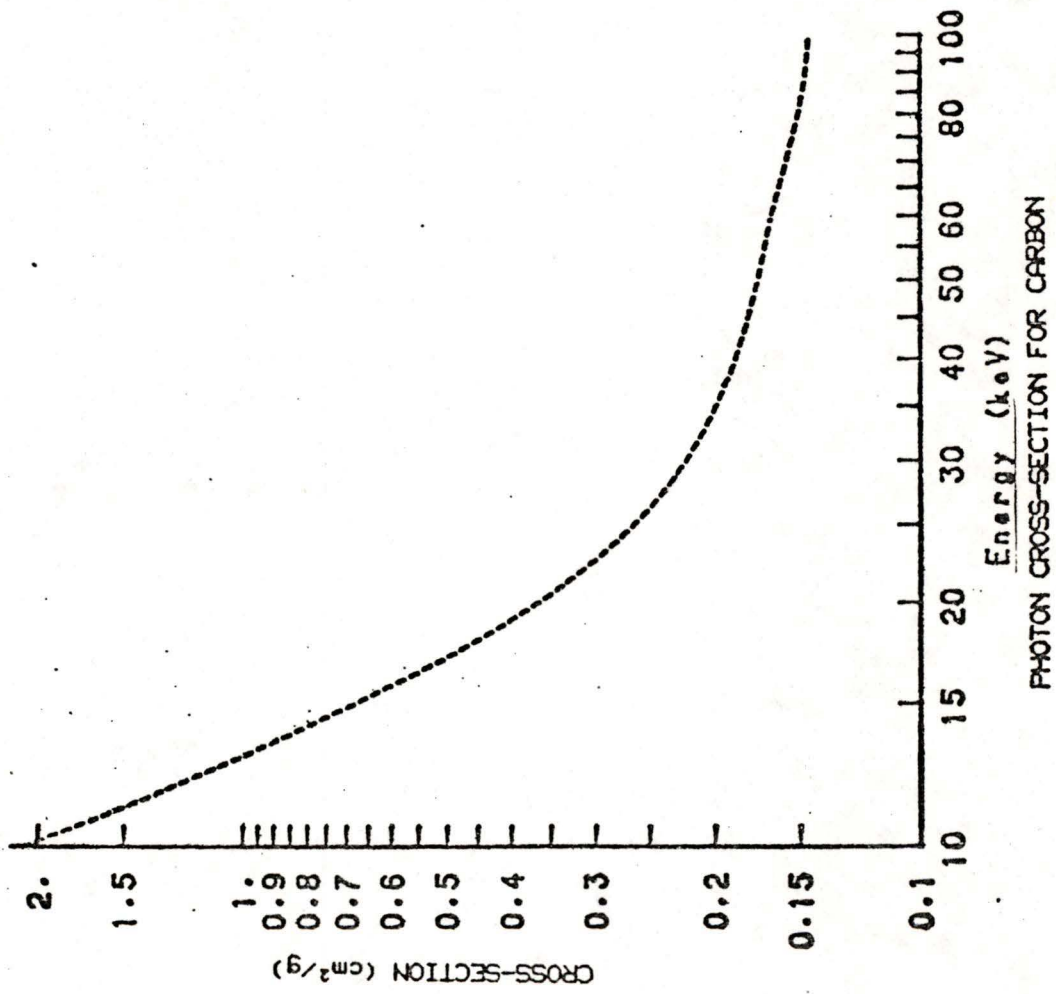
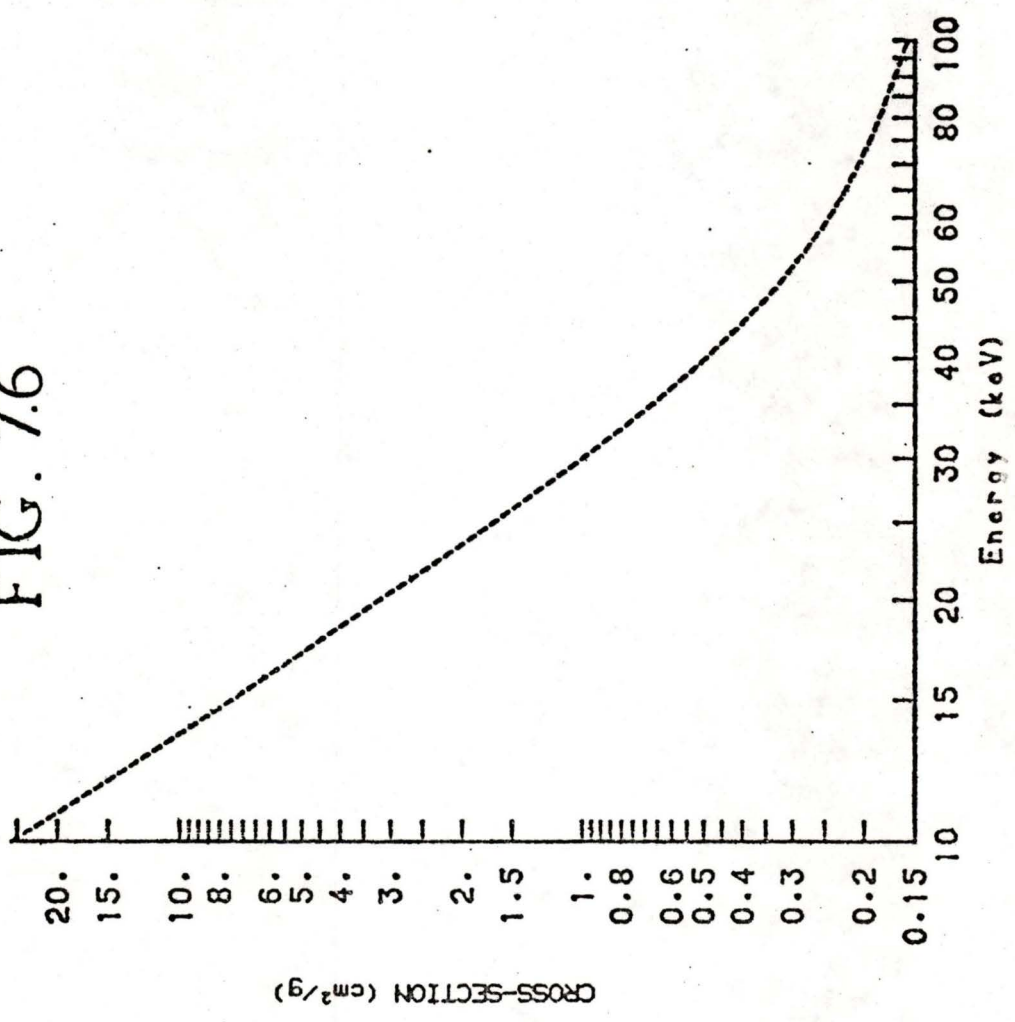


FIG. 7.6



PHOTON CROSS-SECTION FOR ALUMINUM

Chapter 8

Summary and Conclusions

Our measurements of the X rays from pionic ^{12}C and ^{13}C together with previous such measurements are summarised below:

Transition	Energy (keV)	Width(keV)	Reference
$\pi^{12}\text{C}$ 2p-1s	93.287 (43)	2.66(12)	present work
	93.3 (5)	2.6 (5)	Jenkins, 1966
	92.94 (15)	2.96 (15)	Backenstoss, 1967
	93.19 (12)	3.25 (25)	Harris, 1968
$\pi^{12}\text{C}$ 3d-2p	18.400 (6)	.00117 (11)	present work
	18.402 (2)		Egidy, 1974
		.00102 (29)	Koch, 1969
$\pi^{13}\text{C}$ 2p-1s	92.227 (27)	2.59 (11)	present work
	3d-2p 18.427 (2)	.00097 (10)	present work

Comparison of our results for the $\pi^{12}\text{C}$ 2p-1s transition energy and width with previous measurements shows good agreement. It should be noted that none of the previous measurements included low energy exponential tailing of the detector response function in the fit of the 2p-1s X ray. This accounts for the apparent tendency of the previous measurements to report somewhat higher widths and lower energies. The inclusion of the 1.11% natural abundance of ^{13}C is also responsible for a slight shift of our result to higher energy and a decrease in the fitted width (see Section 6.1).

The results obtained for the $\pi^{13}\text{C}$ 2p-1s energy and width benefitted from the relatively larger number of X rays counted in the ^{13}C spectrum than in the ^{12}C spectrum. The intensity of $\pi^{12}\text{C}$ X rays observed as contamination in the ^{13}C spectrum was estimated as $(.6 \pm .3)\%$ the intensity of the $\pi^{13}\text{C}$ X rays (see Chapter 5). This shows that the three scintillator modification of the more usual four scintillator telescope (see Chapter 2) is an effective means of reducing $\pi^{12}\text{C}$ contamination, however, an increase in the intensities of X rays from air and other objects in or near the experiment is inevitable with such a configuration.

The fits of the $\pi^{12}\text{C}$ X-ray L-series give relative intensities which agree with the previous measurements for a graphite target (see Table XV). The $\pi^{12}\text{C}$ 3d-2p transition energy and width also agree with previous measurements. This agreement corroborates the accuracy of the energy and efficiency calibration processes. The relative intensities of the X rays from the pionic L-series of powdered ^{13}C and the energy and width of the $\pi^{13}\text{C}$ 3d-2p transition are the first such measurements to be reported.

Appendix A

Low Energy Exponential Tailing

Photons incident on the germanium detector may, for a variety of reasons, be detected as having energies less than their true values. The probability of registering a photon at lower energy than its true photopeak energy is manifest by "tails" on the lower energy side of the peaks in the spectra, extending to zero energy. The processes responsible for the formation of low energy exponential tails are not well understood.

A.1 Mathematical Formulation

A low energy exponential tail is described mathematically by a probability density $p(E)$ of detecting a photon with energy E_0 as having energy $E < E_0$ which is an exponential form:

$$p(E) = \alpha \exp[-\beta(E_0 - E)] \quad \dots(A.1)$$

Integrating over all energies less than E_0 , one obtains the total probability R resident in the tail from a delta function of unit amplitude:

$$\begin{aligned} R &= \int_0^{E_0} \alpha \exp[-\beta(E_0 - x)] dx \\ &= \alpha (1 - \exp[-\beta E_0]) / \beta \\ &\approx \alpha / \beta \quad \text{for } \beta E_0 \gg 1 \quad \dots(A.2) \end{aligned}$$

R is the ratio of the tail area to the total peak area. A result similar to (A.2) can be derived for the discrete case.

In practice, a discrete form of equation A.1 is used:
 $p(E)$ becomes $P(k)$ where

$$P(k) = \alpha \exp[-\beta(x_0 - x_k)] \quad \dots(A.3)$$

The constant β is redefined in units of channels⁻¹, x_0 is the channel corresponding to the energy E_0 , and x_k the channel in which the count is histogrammed.

In order to use the expression for $P(k)$ in fits it must be convoluted with the Gaussian detector response function (see Section 3.1.1), and the theoretical distribution of incident photon energies. Such a convolution is most easily performed after calculation of the fitting function without tailing. If the fitting function at the k th channel, not including background, is Y_k then the total exponential tail T_k , from all channels $j > k$ is:

$$T_k = \sum_{j=k}^{\infty} Y_j \alpha \exp[-\beta(j-k)] \quad \dots(A.4)$$

Calculation of A.4 for each value of k in the fitting region is time consuming. Instead the following recursion relation is deduced from A.4:

$$T_k = \alpha Y_k + \exp[-\beta] T_{k+1} \quad \dots(A.5)$$

This permits the calculation of T_k simultaneously with the evaluation of Y_k at each channel by starting at the uppermost channel M in the fitting region with an assumed value for T (usually 0) and stepping down through the fit region, channel

by channel.

In the special case of tailing from a purely Gaussian peak, having the form given by equation 3.1, an analytic form can be derived for the exponential tail $T(x)$ by performing the following integral:

$$T(x) = \int_x^{\infty} \alpha \gamma \exp\{-\beta(t-x)\} \exp\{-(t-x_0)^2/(2\sigma^2)\} dt \quad \dots (A.6)$$

The integration is performed by completing the square in the exponential arguments with the following result:

$$T(u) = \frac{\alpha \gamma \sigma \pi^{1/2}}{2^{1/2}} \exp\{\rho u + \rho^4/4\} \operatorname{erfc}(u/\rho + \rho^2/2) \quad \dots (A.7)$$

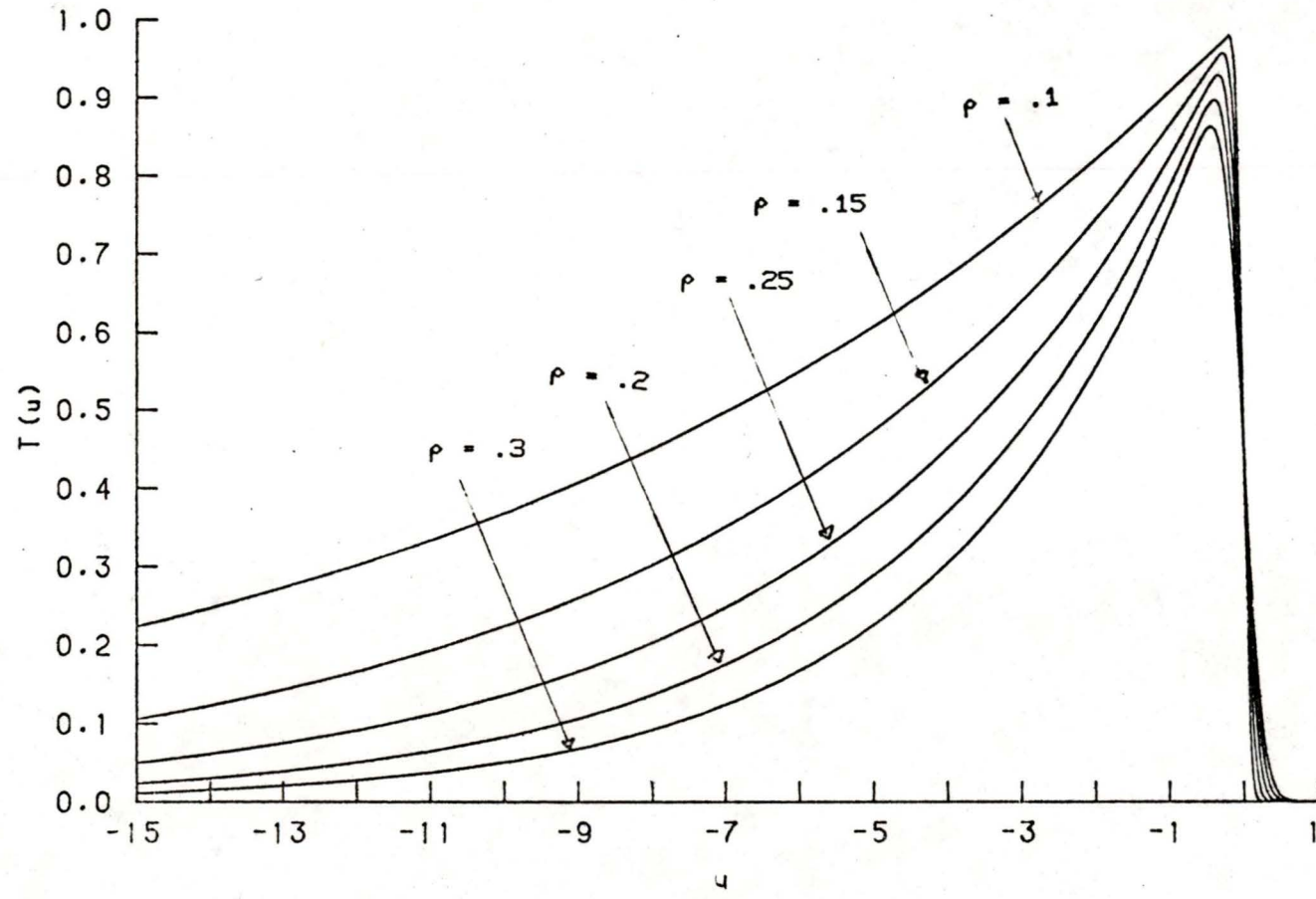
where $u = 2^{-1/4}(\beta/\sigma)^{1/2}(x-x_0)$, $\rho = 2^{1/4}\sigma^{1/2}\beta^{1/2}$, and erfc is the complementary error function. Letting the area of the Gaussian peak be A , equation A.7 becomes:

$$T(u) = \alpha A \exp\{\rho u + \rho^4/4\} \operatorname{erfc}(u/\rho + \rho^2/2)/2 \quad \dots (A.8)$$

where $A = (2\pi)^{1/2}\sigma\gamma$. A graph of A.8 with αA set to unity is shown in figure A.1. The maximum amplitude of the tail is slightly less than unity, occurring near $u = -\rho^3/2$. The height of the tail from a real peak with area A is slightly less than the value of αA .

The implementation of the low energy exponential tailing in the fitting program is further discussed in Appendix C.

FIG. A.1



$T(u)$ for Various Values of ρ

Appendix B

Muonic X-ray 2p-1s Transition Energies and r.m.s. Charge Radii.

In addition to pionic X rays, muonic X rays were observed in the pion spectra for reasons discussed in Chapter 5. It was possible to fit these muonic X rays in some cases and to obtain accurate estimates of the energies of certain muonic 2p-1s transitions and r.m.s. nuclear charge radii.

In particular, the 2p-1s X rays from muonic ^{12}C , ^{13}C , and ^{14}N were observed and fit using the procedures described in Chapters 3 and 6. The energies and radii thus obtained are as follow:

Transition	Energy (keV)	$\langle r^2 \rangle^{1/2}$ (fm)
$\mu^{12}\text{C}$ 2p-1s	75.251 \pm .015	2.51 \pm .05
$\mu^{13}\text{C}$ 2p-1s	75.303 \pm .015	2.51 \pm .05
$\mu^{14}\text{N}$ 2p-1s	102.492 \pm .004	2.579 \pm .003

Allowance was made for ^{12}C contamination of (10 \pm 3)% in the $\mu^{13}\text{C}$ 2p-1s peak (see Chapter 5). The $\mu^{14}\text{N}$ 2p-1s energy was determined from X rays observed from air during the $\pi^{13}\text{C}$ run. Using the observed energies, and vacuum polarization corrections for the various levels (Engfer, 1974), it was possible to extract the energy shift ΔE due to the finite size of the nucleus. The r.m.s. charge radius of the nucleus was then calculated using a method due to Friar (1979), implemented in the FORTRAN code MUON (Poffenberger, 1980). The leading term

in the calculation is due to the overlap of the muon wavefunction with that of the nucleus, given by:

$$\Delta E = \frac{2\pi}{3} Z\alpha |\phi_n(0)|^2 (\langle r^2 \rangle + \text{higher order terms}) \dots (\text{B.1})$$

where ΔE is the energy shift due to the finite extent of the nucleus, Z is the nuclear charge, α is the fine structure constant, and $\langle r^2 \rangle$ is the square of the charge radius. $|\phi_n(0)|^2$ is the square of the n th state non-relativistic muon wavefunction and is equal to:

$$|\phi_n(0)|^2 = (Z\alpha\mu)^3 / (\pi n^3) \dots (\text{B.2})$$

μ is the reduced mass of the muonic atom.

Appendix C

Modifications to the FORTRAN Code JAGSPOT

C.1 Low Energy Exponential Tailing Function 3

Low energy exponential tailing of the form described in Appendix A was implemented in the subroutine AUX of the fitting program JAGSPOT (Olin, 1978). The method uses the recursion relation A.5, calculating not only the value of the exponential tail T at each channel k, but also the derivatives of T with respect to the free parameters in the fit. Noting that the parameters α and β used in the discussion in Appendix A correspond to the parameters a_{25} and a_{26} in JAGSPOT (also referred to as EXT1 and EXT2 respectively) a background function b is calculated for the fit:

$$b_k = a_1 + a_2 x_k + T_k$$

The function T is defined at the k th channel in the fitting region by the application of the recursion relation:

$$T_k = a_{27} \quad (\text{for the maximum value of } k)$$

$$a_{25} Y_k + \exp(-a_{26}) T_{k+1} \quad (\text{otherwise})$$

The derivatives are also calculated recursively, according to the following rules:

$$\frac{\partial T_k}{\partial a_{25}} = 0 \quad (\text{for the maximum value of } k)$$

$$Y_k + \frac{\partial T_{k+1}}{\partial a_{25}} \exp(-a_{26}) \quad (\text{otherwise})$$

$$\frac{\partial T_k}{\partial a_{26}} = 0 \quad (\text{for the maximum value of } k)$$

$$-\exp(-a_{26})T_{k+1} + \exp(-a_{26}) \frac{\partial T_{k+1}}{\partial a_{26}} \quad (\text{otherwise})$$

$$\frac{\partial T_k}{\partial a_{27}} = 1 \quad (\text{for the maximum value of } k)$$

$$\exp(-a_{26}) \frac{\partial T_{k+1}}{\partial a_{27}} \quad (\text{otherwise})$$

For the various parameters of the fit, upon which Y_k depends, the derivatives are (for $j=3,5$ to 24 , and $28,29,30$):

$$\frac{\partial T_k}{\partial a_j} = 0 \quad (\text{for the maximum value of } k)$$

$$a_{25} \frac{\partial Y_k}{\partial a_j} + \exp(-a_{26}) \frac{\partial T_{k+1}}{\partial a_j} \quad (\text{otherwise})$$

The main difference between tailing function 3, described here, and the tailing function 2 which had been used before function 3 was implemented is that Y_k in tailing function 2 is the value of the data less the linear background however, in the case of function 3, Y_k is the value of the fitting function less the linear part of the background. Another difference is that function 3 uses the parameter a_{27} to estimate tailing counts originating outside the fitting region, while function 2 does not use this parameter.

C.2 Low Energy Exponential Tailing Function 4

Using the result A.2 that the ratio of tail area to peak area R is given by the ratio a_{25}/a_{26} , tail function 4 allows exponential tails to be fit with the value of R fixed. The value of R is determined from the ratio of the initial values of a_{25} (EXT1) and a_{26} (EXT2) supplied to the program by the user. The parameter a_{26} should not be a free parameter of the fit however, since its value is calculated from the current value of a_{25} during each iteration of the fitting program. The derivatives of the fitting function with respect to a_{25} are corrected for the extra dependence introduced by forcing $a_{26} = a_{25}/R$.

C.3 The LINK Command

The command LINK has been implemented in the program JAGSPOT to allow parameters describing peak positions and peak amplitudes to be fitted with, in the case of peak positions, the difference in positions as a fixed quantity or, in the case of peak amplitudes, the ratio of the amplitudes as a fixed quantity. The fitting program adjusts linked parameters in unison, just as if they were a single parameter. It is important to realize that when a parameter or parameters are linked to a single parameter, only the single parameter to which the links are made is allowed to vary in the fitting process.

In the case of Gaussian peaks, linking amplitudes is equivalent to linking areas since all peaks of this type have the same FWHM (in the present program). This, however, is not the case

in general: for example linking the amplitudes of Lorentzians does not link their areas since the true amplitude of a such a peak depends upon the Lorentz width as well as the parameter γ (see equation 3.3).

The LINK command may be placed in a JAGSPOT command file in any position preceding the PFIT command. It is usual to put it just before the FUNC command. The two lines following the LINK command must each contain ten integers (in free format). The first line of integers specifies the linking of peak positions, the second specifies the linking of peak amplitudes. In each line a number appears for each of the ten possible peaks in the fit. The first integer corresponds to the first peak, the second to the second peak, and so on. If the n th integer in a line is equal to n , no link is performed. If, on the other hand, the n th integer is not equal to n , instead say to k , then the n th peak is linked to the k th peak.

For example the following sequence of lines would link the position of peak number 5 to that of peak number 3, the position of peak number 7 to that of peak number 8, and the amplitude of peak number 5 to that of peak number 3:

```
LINK
1 2 3 4 3 6 8 8 9 10
1 2 3 4 3 6 7 8 9 10
```

Any peak parameter whose number does not appear in the two lines following the LINK command must be held fixed in the fit.

Bibliography

R. Abela, G. Backenstoss, M. Izycki, W. Kowald, I. Schwanner, L. Tauscher, H.J. Weyer, M. Doerr, W. Fetscher, R. Guigas, D. Gotta, H. Poth, G. Schmidt, and H. Ullrich, ISOTOPIEEFFEKTE AN LEICHTEN PIONISCHEN ATOMEN, *Helvetica Physica Acta*, 52 (1979) 413.

G. Backenstoss, S. Charalambus, H. Daniel, H. Koch, G. Poelz, H. Schmitt, and L. Tauscher, PIONIC 2p-1s TRANSITIONS, *Physics Letters B*, 25 (1967) 365.

G. Backenstoss, I. Bergstrom, J. Egger, R. Hagelberg, C.J. Herrlander, H. Koch, H.P. Povel, R.H. Price, A. Schwitter, and L. Tauscher, *Nuclear Physics B*, 66 (1973) 125.

G. Backenstoss, J. Egger, T. von Egidy, R. Hagelberg, C.J. Herrlander, H. Koch, H.P. Povel, A. Schwitter, and L. Tauscher, PIONIC AND MUONIC X-RAY TRANSITIONS IN LIQUID HELIUM, *Nuclear Physics A*, 232 (1974) 519.

J. Bailey, A. Placci, E. Polacco, E. Zavattini, K. Ziock, G. Carboni, U. Gastaldi, G. Gorini, G. Neri, and G. Torelli, MEASUREMENTS OF PIONIC X-RAYS FROM HYDROGEN, *Physics Letters B*, 33 (1970) 369.

J. Bailey, D.V. Bugg, U. Gastaldi, P. Hattersley, D.R. Jeremiah, E. Klempt, K. Neubecker, E. Polacco, and J. Warren, THE π D SCATTERING LENGTH FROM $K\alpha$ X-RAYS, *Physics Letters B*, 50 (1974) 403.

T. von Egidy and H.P. Povel, L- AND M- SERIES IN CARBON AND OXYGEN AND THE PIONIC 2p LEVEL SHIFT AND WIDTH OF OXYGEN, *Nuclear Physics A*, 232 (1979) 511.

R. Engfer, H. Schneuwley, J.L. Vaillumier, H.K. Walter, and A. Zehnder, CHARGE DISTRIBUTION PARAMETERS, ISOTOPE SHIFTS, AND MAGNETIC HYPERFINE CONSTANTS FROM MUONIC ATOMS, *Atomic Data and Nuclear Data Tables*, 14 (1974) 509.

J.L. Friar, FINITE SIZE CORRECTIONS TO THE ENERGY LEVELS OF LIGHT MUONIC ATOMS, *Physics Letters B*, 80 (1979) 157.

R.J. Gerhke and R.A. Lokken, CALIBRATION OF THE EFFICIENCY OF A Si(Li) SPECTROMETER IN THE ENERGY REGION 5 TO 125 KEV, *Nuclear Instruments and Methods*, 97 (1971) 219.

R.J. Gerhke, R.G. Helmer, and R.C. Greenwood, PRECISE RELATIVE γ -RAY INTENSITIES FOR CALIBRATION OF Ge SEMICONDUCTOR DETECTORS, Nuclear Instruments and Methods, 147 (1977) 405.

J.S. Hansen, J.C. McGeorge, D. Nix, W.D. Schmitt-Ott, I. Unus, and R.W. Fink, ACCURATE EFFICIENCY CALIBRATION AND PROPERTIES OF SEMICONDUCTOR DETECTORS FOR LOW ENERGY PHOTONS, Nuclear Instruments and Methods, 106 (1977) 365.

R.J. Harris Jr., W.B. Shuler, M. Eckhause, R.T. Siegel, and R.E. Welsh, ENERGY AND WIDTH MEASUREMENTS OF LOW Z PIONIC X-RAY TRANSITIONS, Physical Review Letters, 20 (1968) 505.

R.G. Helmer, R.C. Greenwood, and R.J. Gerhke, REEVALUATION OF PRECISE γ -RAY ENERGIES FOR CALIBRATION OF Ge(Li) SPECTROMETERS, Nuclear Instruments and Methods, 155 (1978) 189.

D.A. Jenkins, R. Kunselman, M.K. Simmons, and T. Yamazaki, $2p-1s$ TRANSITIONS IN π -MESONIC ATOMS, Physical Review Letters, 17 (1966) 1.

KeveX Corporation, ALL YOU EVER WANTED TO KNOW ABOUT X-RAY ENERGY SPECTROMETRY, Burlingame, California (1973).

H. Koch, MUONIC AND HADRONIC ATOMS, Nuclear and Particle Physics at Intermediate Energies, p. 87, ed. J.B. Warren, Plenum Press (1975).

H. Koch, M. Krell, Ch.V.D. Malsburg, G. Poelz, H. Schmitt, L. Tauscher, G. Backenstoss, S. Charalambus, and H. Daniel, PIONIC $2p$ LEVEL WIDTHS IN LIGHT NUCLEI, Physics Letters B, 29 (1969) 140.

M. Krell, THE PIONIC (KAONIC) ATOM PROGRAM: PIATOM, University of Victoria, TRIUMF report VP-77-5.

G.R. Mason, G.A. Beer, M.S. Dixit, S.K. Kim, J.A. MacDonald, A. Olin, R.M. Pearce, W.C. Sperry, and J.S. Vincent, PRECISE MEASUREMENT OF PIONIC K X RAYS IN LIQUID ^3He , Nuclear Physics A, 340 (1980) 240.

L.F. Mausner, CHEMICAL EFFECTS ON THE ATOMIC CAPTURE OF NEGATIVE MUONS, Ph.D. Thesis, unpublished; Princeton (1975).

A. Olin, JAGSPOT: A CODE FOR FITTING COMPLEX GAMMA RAY SPECTRA, University of Victoria TRIUMF report VPN-78-2.

A. Olin, P.R. Poffenberger, G.A. Beer, J.A. MacDonald, G.R. Mason, R.M. Pearce, and W.C. Sperry, MEASUREMENT OF PIONIC AND MUONIC X RAYS IN 10,11 BORON, to be published (1980).

P. Poffenberger, FORTRAN CODE MUON, University of Victoria, unpublished (1980).

H. Poth, A COMPILATION OF DATA FROM HADRONIC ATOMS, Physics Data, 14 (1979)

I. Schwanner, R. Abela, G. Backenstoss, W. Kowald, P. Pavlopoulos, L. Tauscher, H.J. Weyer, P. Blum, M. Doerr, W. Fetscher, D. Gotta, R. Guigas, H. Koch, H. Poth, G. Schmidt, and H. Ullrich, ISOTOPE EFFECTS IN LIGHT PIONIC ATOMS, to be published.

E. Storm and H.I. Israel, PHOTON CROSS-SECTIONS, Nuclear Data Tables A, 7 (1970) 565.

VITA

Surname: Fry

Given names: Charles Alan

Place of Birth: Ottawa, Ont. Date of Birth: 26 May 1953

Educational Institutions Attended, with Dates of Entering and Leaving:

University of Victoria, Victoria, B.C. 1971 to 1973

Keio University, Tokyo, Japan 1973 to 1974

University of Victoria, Victoria, B.C. 1974 to 1976

University of Victoria, Victoria, B.C. 1977 to 1980

Degrees, Diplomas, etc., Awarded with Dates and Names of Institutions:

B.Sc., 1976, University of Victoria, Victoria, B.C.

Honours and Awards:

University of Victoria Graduate Fellowship 1978-1979

University of Victoria Graduate Fellowship 1979-1980

Publications and Papers Presented at Scientific Meetings:

C.A. Fry et al., PIONIC X RAYS FROM $^{12,13}\text{C}$, Proceedings of the Western Regional Nuclear Conference, Hecla Island, February, 1980.


A. Olin et al., STRONG INTERACTION SHIFTS AND WIDTHS IN PIONIC $^{10,11}\text{B}$ AND $^{12,13}\text{C}$, Proceedings of the 8th ICOHEPANS, Vancouver, August, 1979.

PARTIAL COPYRIGHT LICENSE

I hereby grant the right to lend my thesis, the title of which is shown below, to users of the University of Victoria Library, and to make single copies only for such users or in response to a request from the library of any other university or similar institution, on its behalf or one of its users. I further agree that permission for extensive copying of this thesis for scholarly purposes may be granted by me or a member of the University designated by me. It is understood that copying or publication of this thesis for financial gain shall not be allowed without my written permission.

PIONIC X RAYS FROM ^{12}C and ^{13}C

Author


Alan Fry

July, 1980